

# A Full $w$ CDM Analysis of KiDS-1000 Weak Lensing Maps using Deep Learning

Janis Fluri<sup>a,b,\*</sup>, Tomasz Kacprzak<sup>a,c</sup>, Aurelien Lucchi<sup>d</sup>, Aurel Schneider<sup>e</sup>, Alexandre Refregier<sup>a</sup>, and Thomas Hofmann<sup>b</sup>

<sup>a</sup>*Institute of Particle Physics and Astrophysics, Department of Physics, ETH Zurich, Switzerland*

<sup>b</sup>*Data Analytics Lab, Department of Computer Science, ETH Zurich, Switzerland*

<sup>c</sup>*Swiss Data Science Center, Paul Scherrer Institute, Switzerland*

<sup>d</sup>*Department of Mathematics and Computer Science, University of Basel and*

<sup>e</sup>*Center for Theoretical Astrophysics and Cosmology,*

*Institute for Computational Science, University of Zurich, Switzerland*

(Dated: April 21, 2022)

We present a full forward-modeled  $w$ CDM analysis of the KiDS-1000 weak lensing maps using graph-convolutional neural networks (GCNN). Utilizing the COSMOGRID, a novel massive simulation suite spanning six different cosmological parameters, we generate almost one million tomographic mock surveys on the sphere. Due to the large data set size and survey area, we perform a spherical analysis while limiting our map resolution to HEALPix  $n_{\text{side}} = 512$ . We marginalize over systematics such as photometric redshift errors, multiplicative calibration and additive shear bias. Furthermore, we use a map-level implementation of the non-linear intrinsic alignment model along with a novel treatment of baryonic feedback to incorporate additional astrophysical nuisance parameters. We also perform a spherical power spectrum analysis for comparison. The constraints of the cosmological parameters are generated using a likelihood-free inference method called Gaussian Process Approximate Bayesian Computation (GPABC). Finally, we check that our pipeline is robust against choices of the simulation parameters. We find constraints on the degeneracy parameter of  $S_8 \equiv \sigma_8 \sqrt{\Omega_M/0.3} = 0.78_{-0.06}^{+0.06}$  for our power spectrum analysis and  $S_8 = 0.79_{-0.05}^{+0.05}$  for our GCNN analysis, improving the former by 16%. This is consistent with earlier analyses of the 2-point function, albeit slightly higher. Baryonic corrections generally broaden the constraints on the degeneracy parameter by about 10%. These results offer great prospects for full machine learning based analyses of on-going and future weak lensing surveys.

## I. INTRODUCTION

The large scale structures (LSS) of the Universe contains a wealth of information that can be used to test our cosmological models. Weak gravitational lensing (WL) (see e.g. [1, 2] for reviews) utilizes the laws of general relativity along the shape measurements of millions of galaxies to reconstruct the projected matter distribution of the Universe. The unique ability of WL to directly observe the matter contents of the Universe makes it an ideal probe to constrain cosmological parameters. This has already been demonstrated by WL surveys such as the Canada France Hawaii Telescope Lensing Survey (CFHTLenS)[3] [4], the Kilo-Degree Survey (KiDS)[5] [6, 7], the Dark Energy Survey (DES)[8] [9, 10], and the Subaru Hyper Suprime-Cam (HSC)[11] [12]. Future surveys such as Euclid [13], the Vera C. Rubin Observatory [14] or the Wide-Field Infrared Survey Telescope (WFIRST) [15] will be able to provide even more precise measurements.

On large scales, the projected matter distribution of the Universe approximately follows the distribution of a Gaussian random field, making statistics based on the two-point correlation function ideal tools to analysis the of data [7, 9, 12]. However, the increasing quality and quantity of the available data makes it possible to probe scales, where the evolution of the matter distribution is

dominated by non-linear effects, leading to information that cannot be fully extracted by the two-point correlation function alone. This motivates the search for novel summary statistics with the ability to extract non-Gaussian information. Such approaches include weak lensing peak statistics (e.g. [10, 16–23]), the three-point correlations function (e.g. [24, 25]) or machine learning based methods (e.g. [26–30]). These higher order statistics have the potential to greatly improve the cosmological parameter constraints and reduce the systematic effects. However, one problem is that analytical predictions are typically not available, making it necessary to predict them with costly simulations. Additionally, the common assumption of a Gaussian likelihood might break down for complicated statistics and likelihood-free inference methods may have to be used.

In this work we perform a forward-model  $w$ CDM machine-learning analysis of the KiDS-1000 data [31] using very similar settings as the KiDS-1000 two-point correlation function analysis [7, hereafter A20]. To achieve this we build upon our previous analysis of the KiDS-450 data [29, hereafter F19], but significantly improve the pipeline by increasing the number of cosmological and nuisance parameters, as well as using a different type of neural networks along with the likelihood-free inference method Gaussian Process Approximate Bayesian Computation (GPABC) [28] to constrain the cosmological parameters. Similar to F19 we perform an analysis based on neural networks as well as a standard power spectrum analysis for comparison. In contrast to F19,

\* janis.fluri@phys.ethz.ch

we do not need to cut the observed data in independent patches, and instead treat the whole survey at once on the sphere. We create the necessary mock surveys for the evaluation of the power spectra and the training of the networks using the UFALCON [32, 33] software and a novel simulations suite, called the COSMOGRID [34]. The COSMOGRID is an extensive simulation suite that contains  $\sim 20'000$  independent simulations of  $2'500$  distinct parameter combinations of the  $w$ CDM model, varying 6 cosmological parameters, namely the total matter density  $\Omega_M$ , the fluctuation amplitude  $\sigma_8$ , the spectral index  $n_s$ , the Hubble parameter  $H_0 \equiv 100h$ , the baryon density  $\Omega_b$ , and the dark energy equation of state parameter  $w_0$ . The large size of the COSMOGRID poses computational challenges and we therefore limit the resolution of our mock surveys to a HEALPix  $n_{\text{side}} = 512$ . Our generated mock surveys incorporate systematics such as photometric redshift errors or the multiplicative and additive shear biases in a similar way as A20. Furthermore, we utilize the map-level implementation of the non-linear intrinsic alignment model (NLA) [35–37] presented in F19 to constrain the intrinsic alignment amplitude  $A_{\text{IA}}$ . Additionally, we develop a new method to treat baryonic feedback for the COSMOGRID simulations based on [38–40] that allows us to marginalize over baryonic effects. We evaluate the power spectrum of the generated, spherical mock surveys and further analyse them with graph-convolutional neural networks utilizing DEEPSHERE [41] and an information maximizing loss [28, 42]. Finally, we perform a likelihood-free parameter inference using GPABC [28].

This paper is structured as follows. In section II we give an overview of the used data. In section III we describe our blinding scheme. Section IV contains a detailed description of our methods, including the mock survey generation, treatment of all systematics, the used networks and our inference pipeline. We discuss our tests of the whole pipeline with respect to simulation settings in section V and present our results in section VI, which is followed by our conclusions in section VII. Afterwards, appendix A includes more details about certain prior choices. In appendix B we present tests for the accuracy of our mock surveys and in appendix C we describe our baryon model in more detail. More information and tests for our examined networks are presented in appendix D and finally, our full parameter constraint can be found in appendix E.

## II. KIDS-1000 DATA

In this work, we analyse the fourth data release [31] of the Kilo-Degree Survey (KiDS [43]) which is a public survey by the European Southern Observatory (ESO). This release contains  $\sim 1000 \text{ deg}^2$  of images giving it the name KiDS-1000. KiDS is observing in four band ( $ugri$ ) using the OmegaCAM CCD mosaic camera mounted at the Cassegrain focus of the VLT Survey Telescope (VST). This combination was designed to have a well-behaved

and almost round point spread function (PSF), as well as a small camera shear, making it ideal for weak lensing measurements. The combination with its partner survey, VIKING (VISTA Kilo-degree INfrared Galaxy survey [44]), increases the number of observed optical and near infrared bands of the galaxies to nine ( $ugriZJHK_s$ ), greatly improving their photometric redshift estimates. The observed data is processed with the two pipelines THELI [45] and ASTRO-WISE [46] and the galaxy shear estimates are obtained with LENSFIT [47, 48]. LENSFIT uses a likelihood-based method to fit a disc and bulge model to each of the observed galaxies to extract their shear values. Each galaxy is also assigned a weight based on this likelihood, with large weight indicating a high confidence of the fit. Additionally, photometric redshifts of the galaxies are obtained using the BPZ code [49]. A detailed description of the KiDS-1000 methodology can be found in [50].

### A. Data Preparation

We split the galaxies into five tomographic bins using their BPZ estimated in the same way as in A20. The most important quantities of these bins can be found in table 1 of A20. To create shear maps from the observed galaxies, we project them onto HEALPix [51] maps with a resolution of  $n_{\text{side}} = 512$ . However, before the projection, we rotate the positions of the galaxies, as well as their shear values. This rotation is performed to increase the number of cutouts that can be obtained from simulated maps as described in section IV B and is visualized in Figure 1. After the rotation, the shear value of each pixel is calculated as the weighted mean of the shear values  $e_i$  of the galaxies inside the pixel

$$\gamma_{\text{pix}} = \frac{\sum_{i \in \text{pix}} w_i (e_i - c_z)}{\sum_{i \in \text{pix}} w_i}, \quad (1)$$

where the  $w_i$  are the LENSFIT weights and the constants  $c_z$  are chosen such that the weighted mean shear of each redshift bin is zero (see section IV E 2).

## III. BLINDING

The analysis presented in this work was performed in a blinded fashion to avoid a confirmation bias. The shear values of the observed galaxies were only used to generate noise footprints in the analysis pipeline (see section IV C). We only unblinded the actual observed data after two conditions were met. First, the power spectra analysis (see section IV H 1) had to be consistent with the network analysis (see section IV H 2). Second, the analysis had to be robust against the simulation settings used for the data generation (see section V). The observed data was only analyzed after passing both of these requirements. After the unblinding we did not change our analysis pipeline.

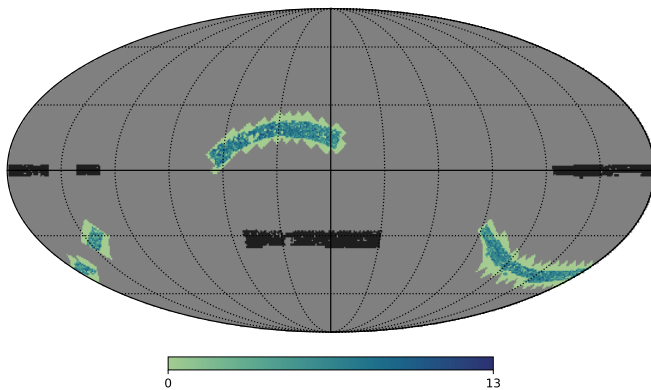


FIG. 1. The original KiDS-1000 survey footprint is shown in dark grey and the galaxy density [galaxies/arcmin<sup>2</sup>] of the rotated footprint in blue. The pixels with zero galaxies are part of the padding necessary to process the maps with the graph convolutional neural network (see section IV F) and not part of the original survey.

However, we did run an additional analysis, where we adapted a hyperparameter of our inference method. This is explained in more details in section VI.

## IV. METHODOLOGY

An overview of the data flow is given by Figure 2. The depicted flowchart explains most of the crucial parts of the data generation procedure. Additional parts of the pipeline that are not shown include our handling of the photometric redshift error (see section IV E 1), our treatment of baryonic effects (see section IV E 4), details about the used networks (see sections IV F and IV G) and, finally, our inference method (see section IV H).

### A. Simulations

#### 1. Parameters

The training of the GCNN as well as the inference of the cosmological parameters requires a tremendous amount of simulations. In this work, we use the COSMOGRID [34] to generate the necessary weak lensing maps. The COSMOGRID is a simulation suite generated with the fast and efficient PKDGRAV3 code [52]. It contains seven independent simulations for each of the 2'500 grid cosmologies varying six different cosmological parameters, as well as, 200 distinct simulations of a fiducial cosmology and perturbations of it. The perturbed fiducial simulations are simulations for which a single cosmological parameter  $\theta$

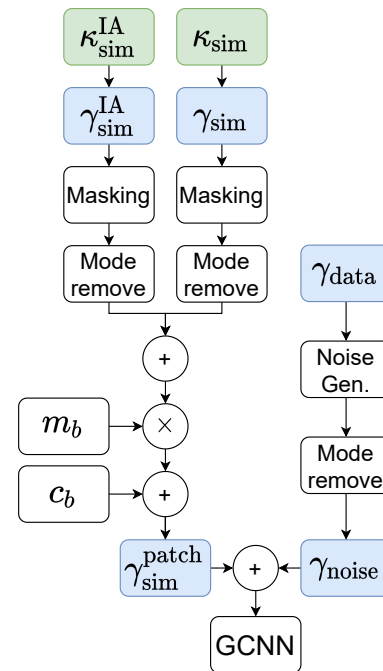


FIG. 2. Overview of the data flow used in the analysis. Section IV B explains the generation of full sky convergence  $\kappa_{\text{sim}}$  and intrinsic alignment maps  $\kappa_{\text{sim}}^{\text{IA}}$ , as well as, the spherical KS inversion to transform the convergence maps to shear maps  $\gamma_{\text{sim}}$  &  $\gamma_{\text{sim}}^{\text{IA}}$  and the subsequent masking. The mode removal strategy is covered in section IV D. Section IV C describes the generation of noise maps  $\gamma_{\text{noise}}$  from the actual observed data  $\gamma_{\text{data}}$ . Finally, the handling of the multiplicative shear bias  $m_b$  and additive shear bias  $c_b$  is described in section IV E 2.

was changed by a small shift  $\pm\Delta\theta$ , but the seeds of the initial conditions remained unchanged. These simulations can be used to estimate derivatives of quantities with respect to the cosmological parameters via finite difference methods (see e.g. section IV F 1). The six varying cosmological parameters are listed in table I. The dark energy density  $\Omega_\Lambda$  was adapted for each simulation to achieve a flat  $w$ CDM universe and the neutrino mass was fixed to three degenerate neutrinos each having a mass of  $m_\nu = 0.02$  eV. The 2'500 grid points are split into two sub-grids: 1'250 grid points follow a Sobol sequence inside the priors listed in table I and 1'250 grid points follow a Sobol sequence with tighter priors around the fiducial parameters (see e.g. Figure 3), focusing on the region of interest. A Sobol sequence is a quasi-random low-discrepancy sequence that uniformly samples the space. It is similar to Latin hypercube sampling. However, it has the advantage that the sample size does not have to be set in advance, allowing the addition of new samples to the sequence. Another important property is that the number of dimensions of the samples can also be extended, making it easy to add new parameters. One should note that the tight prior is not relevant for this analysis as we only consider the full range of the parameters. The

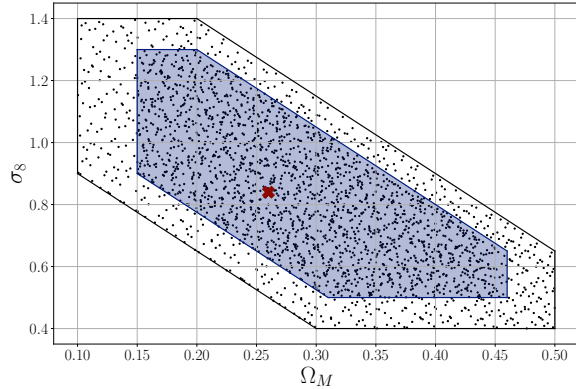


FIG. 3. The 2'500 grid points projected onto the  $\Omega_M - \sigma_8$  plane. The outer boundary shows the additional prior and the shaded region corresponds to the tight prior. The red cross in the middle indicates the fiducial cosmology.

fiducial parameters and their perturbations are also listed in table I.

There are two additional priors not stated in table I. The first one is in the  $\Omega_M - \sigma_8$  plane, shown in Figure 3, and motivated by the degeneracy region of the two parameters. The second one is in the  $\Omega_M - w_0$  plane and caused by the effective nature of the  $w$ CDM model and the relativistic fields in the simulations. More details about this can be found in appendix A.

## 2. Settings

The grid and fiducial simulations were all run with  $832^3$  particles in a box with a side length of 900 Mpc/ $h$ . The simulations also include three degenerate massive neutrinos each having a mass  $m_\nu = 0.02$  eV and general relativistic effects, which are modeled as described in [53]. This model requires a lookup table of highly accurate transfer functions. This table was generated using CLASS [54] and then transformed into the proper N-body gauge using CONCEPT [55]. This lookup table was also used to generate the initial conditions at  $z = 99$ . The remaining precision parameters were left to their default values as in F19.

After the initial condition generation, the simulations used 140 base time steps [56] to evolve the particles to  $z = 0$ . The first 70 time steps were equally spaced in proper time and evolved the particles to  $z = 4$  and the remaining steps were equally spaced in proper time between  $z = 4$  and  $z = 0$ . This split in the evolution was done to reduce the number of steps at low redshifts to reduce the amount of generated data. The simulations were run in lightcone mode and after crossing  $z = 3.5$  a shell of particles with a resolution of  $n_{\text{side}} = 2048$  was generated for each time step, containing the particles that left the observed lightcone. The simulated box was replicated to

cover the relevant range if necessary. PKDGRAV3 also includes a friends-of-friends (FoF) halo finder. For each time step, a halo catalog was generated using a linking length of one-fifth of the mean particle separation. This catalog was later used to include baryonic effects into the generated weak lensing maps (see section IV E 4).

## 3. Benchmarks

Additionally to the fiducial and grid simulations, the COSMOGRID contains different types of benchmark simulations. These simulations were all run using the fiducial cosmology. Each benchmark contains five independent simulations and the random seeds for the initial conditions were the same across the different settings. This was done to reduce the cosmic variance between the different benchmarks, which makes it easier to use them to test various systematics. The first benchmark simulations were run with exactly the same parameters as the fiducial simulations. This benchmark can be used to generate mock observations that are equivalent to the other benchmarks in terms of cosmic variance, but run with the normal simulation settings. For the second benchmark the particle count was increased to  $2048^3$ . This can be used to check the convergence of the simulations and with respect to the particle count. For the third benchmark the boxsize was increased to 2250 Mpc/ $h$ , while keeping the particle density the same, which can be used to investigate the effect of modes that are larger than the fiducial setup. The last benchmark was generated to check the redshift resolution of the fiducial setup. For this run, the number of base timesteps was increased to 500, of which 100 were equally spaced in proper time to  $z = 4$  and the remaining 400 were equally spaced between  $z = 4$  and  $z = 0$ . All these benchmarks were used to check the robustness of our pipeline with respect to simulation settings and the results are presented in section V.

## B. Mock surveys

Similarly to F19 and [10], we generate full sky convergence maps with the simulated shells using UFALCON [32, 33]. However, we downgrade the simulated shells to an  $n_{\text{side}}$  of 512 to alleviate the computational costs and reduce the memory consumption of the generated surveys. UFALCON uses the Born approximation to efficiently generate convergence and intrinsic alignment (see section IV E 3) maps. The convergence of any given pixel  $\theta_{\text{pix}}$  is calculated in the following way

$$\kappa(\theta_{\text{pix}}) \approx \frac{3}{2} \Omega_m \sum_b W_b \frac{H_0}{c} \int_{\Delta z_b} \frac{cdz}{H_0 E(z)} \delta(\vec{v}_{\text{pix}}, z),$$

where  $\mathcal{D}(z)$  is the dimensionless comoving distance and the vector  $\vec{v}_{\text{pix}}$  is given by

$$\vec{v}_{\text{pix}} = \frac{c}{H_0} \mathcal{D}(z) \hat{n}_{\text{pix}}.$$



$\theta$	$\theta_{\text{fid}}$	$\Delta\theta$	Prior
$\Omega_M$	0.26	0.01	[0.1, 0.5]
$\sigma_8$	0.84	0.015	[0.4, 1.4]
$h$	0.6736	0.02	[0.64, 0.82]
$\Omega_b$	0.0493	0.001	[0.03, 0.06]
$n_s$	0.9649	0.02	[0.87, 1.07]
$w_0$	-1.0	0.05	[-2.0, -0.333]
$m_\nu$	0.02	N/A	fixed
$A_{\text{IA}}$	0.0	0.1	[-3.0, 3.0]
$\lg(M_c^0)$	13.82	0.1	[12.0, 15.0]
$\nu$	0.0	0.1	[-2.0, 2.0]
$\delta_z$	N/A	N/A	$\mathcal{N}(\mu_z, \mathbf{C}_z)$
$m$	N/A	N/A	$\mathcal{N}(\mu_m, \mathbf{C}_m)$
$\delta_c$	N/A	N/A	$\mathcal{N}(0, 2.3 \times 10^{-4})$

TABLE I. Cosmological and nuisance parameters used in this analysis. We provide the fiducial values  $\theta_{\text{fid}}$  along with their perturbations  $\delta\theta$  used for the training of the network and the MOPED compression (see sections IV F and IV H 1). We vary six cosmological parameters in flat priors and also constrain three astrophysical nuisance parameters: the intrinsic alignment amplitude  $A_{\text{IA}}$  (section IV E 3) and the baryon parameters  $M_c^0$  and  $\nu$  (section IV E 4). The priors of the mean shift of the redshift distributions  $\delta_z$  (section IV E 1) and the multiplicative bias  $m$  are modeled as multivariate Gaussians with means  $\mu_z$  and  $\mu_m$ , and covariance matrices  $\mathbf{C}_z$  and  $\mathbf{C}_m$ . The uncertainty of the additive bias  $\delta_c$  (section IV E 2) is modeled with an univariate Gaussian prior. The parameters  $\delta_z$ ,  $m$  and  $\delta_c$  are marginalized in the analysis and not constrained.

The vector  $\hat{n}_{\text{pix}}$  is a unit vector pointing to the pixels center and  $E(z)$  is given by

$$dD = \frac{dz}{E(z)}. \quad (2)$$

The sum runs over all redshift shells and  $\Delta z_b$  is the thickness of shell  $b$ . Each shell gets the additional weight  $W_b$  which depends on the redshift distribution of the source galaxies. We refer the interested reader to [32, 33] for a detailed description. The generation of the intrinsic alignment maps works in a similar way, but uses different weights for the shells, which is described in F19. The Born approximation used to generate the maps might have an impact on the constraints. However, [57] showed that the impact of the approximation is negligible for stage-III surveys like KiDS, which was also verified by the systematics test in F19.

We generate the maps using the same redshift distributions as A20. A detailed description of the construction of the redshift distributions can be found in [58] and our treatment of the photometric redshift error is described in section IV E 1. It is important to note that these redshift distributions span a range of  $0 \leq z \leq 6$  which is significantly larger than the range of our simulations. However, the lensing contribution of the matter between  $3.5 \leq z \leq 6$  is negligible for KiDS-1000. We therefore used the whole range of the redshift distributions, but ignored the contribution of the matter in the high redshift regime outside of the range of our simulations. We compare the power

spectra of the generated maps to predictions obtained with PyCCL [59] in appendix B.

After generating full sky convergence maps, we used the spherical Kaiser-Squires (KS) inversion [60] to transform them into weak lensing shear maps. This transformation has two unwanted side effects that have to be addressed in the analysis. First, such a transformation acts as a low-pass filter on the maps, because the highest  $\ell$ -mode in the transformation is directly linked to the resolution of the maps and a perfect reconstruction of the original convergence map is not possible. Second, the generated map contains only E-modes. We address these issues after the masking with a “mode removal” (see section IV D) strategy similar to the one used in F19.

After the first spherical KS inversion, we mask the full sky cosmic shear maps to generate mock surveys. To make better use of the simulated area, we cut out eight survey footprints out of a single simulation. These footprints are shown in Figure 4. Each of the shown footprints can be obtained from the original (rotated) survey footprint (see Figure 1) with a transformation that respects the HEALPix octahedral symmetry, meaning that each pixel can be mapped to exactly one pixel without overlapping with any other pixels. For the grid cosmologies, we generated five full sky convergence maps per patch with a different redshift distribution (see section IV E 1), resulting in 280 (seven simulations  $\times$  eight patches  $\times$  five realizations) mock surveys per grid point after the KS inversion. This results in a total of 700’000 mock surveys for all grid cosmologies combined. For the fiducial cosmology, including its perturbations and benchmarks, we generated a total of ten full sky convergence maps per patch, resulting in 16’000 mock surveys for the fiducial simulations and its perturbations and 400 mock surveys for the benchmarks.

The combined size of all generated mock surveys with a resolution of  $n_{\text{side}} = 512$  is approximately  $\sim 11$  TB, showing the immense size of the data set. Increasing the resolution to  $n_{\text{side}} = 1024$  would increase the memory usage of the mock surveys by a factor of four. Additionally, it would significantly increase the time to train the neural networks and to evaluate the power spectra. We therefore leave the analysis of smaller scales that could be probed with a higher resolution to future work.

At this point the generated mock surveys do not contain any noise and still suffer from the side effects of the KS inversion. Also, they do not include effects of the multiplicative and additive shear bias yet. We will cover all these aspects in the following sections.

### C. Shape and Measurement Noise

The simulation of realistic noise maps is crucial for the analysis. To do this, we use the same technique as in F19 and generate noise maps using random rotations of the

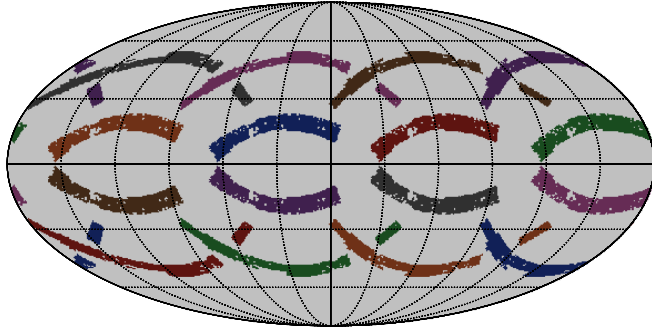


FIG. 4. The eight patches that were to make better use of the full sky simulations. The patches respect the **HEALPix** octahedral symmetry, meaning that one can perfectly map every pixel of each patch onto any other patch without causing unwanted artefacts.

observed shear values

$$\gamma_{\text{pix}}^{\text{noise}} = \frac{\sum_{j \in \text{pix}} \exp(\vartheta_j i) w_j (\gamma_j - c_z)}{\sum_{j \in \text{pix}} w_j}, \quad (3)$$

where the  $\vartheta_j$  are drawn uniformly from  $[0, 2\pi)$ . The rotation and projection of the galaxies is computationally very efficient and could theoretically be done on the fly during the training of the networks. However, noise maps that are generated this way are not band limited and also contain B-modes. Therefore, we have to apply our mode removal (see section IV D) which requires a spherical harmonics decomposition. Such a transformation cannot be done on-the-fly during the training or evaluation of the network and we decided to create a static dataset of noise footprints. We produced one noise map for each generated mock survey of the grid cosmologies and two for each mock survey of the fiducial cosmology, one for the training and one for the evaluation. The generation of two independent noise maps for each mock survey of the fiducial simulations was necessary to avoid overfitting during the training of the network (see section IV F 1).

#### D. Mode Removal

Projecting the shear of the observed galaxies onto a spherical grid leads to shear maps that contain B-modes and are not band-limited. We define a band-limited map as a map that can be decomposed into spherical harmonics without losing information. Theoretically, this is always possible, but it can be numerically unstable. Because of this, **HEALPix** limits the resolution of the spherical harmonics decomposition to modes with  $\ell \leq 3n_{\text{side}} - 1$  per default. Therefore, the simulated shear maps do not have modes above the cutoff scale. However, the projected galaxies from the survey and the noise realizations still

contain these modes, which can potentially lead to biases in the results. Additionally, the simulated convergence maps will produce shear maps that only contain E-modes, as opposed to the observed maps and noise maps, which can contain B-modes. These missing modes can also lead to biases. We mitigate these potential biases by performing an additional spherical harmonic decomposition on all masked maps. During this decomposition we remove all B-modes from the shear maps. This way, all generated simulations, noise maps and the true data are band limited, contain the same masking effects and are E-modes only. We dub this additional decomposition “model removal” (see Figure 2).

#### E. Systematics

In this section we describe our treatment of the systematic effects that we consider in this work. In our analysis we marginalize over photometric redshift errors (section IV E 1), intrinsic alignment (section IV E 3), the multiplicative and additive shear bias (section IV E 2), as well as baryonic feedback (section IV E 4). Furthermore, we check that our results are robust to the simulation settings of the **COSMOGRID** (section IV E 5).

##### 1. Photometric Redshift

The redshift distributions of each tomographic bin of the KiDS-1000 dataset have been calibrated using the self-organising map (SOM) method of [61] with additional requirements described in [62]. The resulting distributions have a reliable mean redshift with a high accuracy coming from the nine-band photometry of the galaxies. The expected uncertainty on the mean redshift was estimated using mock simulations. Following A20, we use the same means and covariance matrix to model the uncertainty on the mean redshifts of the five tomographic distributions as multivariate Gaussians. Each generated mock survey (see section IV B), either for the training or evaluation, has been produced with a redshift distribution that is shifted by a random draw from this multivariate Gaussian to marginalize over the photometric redshift errors.

##### 2. Multiplicative and Additive Shear Bias

We use the common model of an additive and multiplicative shear bias correction to model the calibration uncertainty

$$\gamma^{\text{obs}} = (1 + m_z)\gamma + c_z, \quad (4)$$

where  $m_z$  and  $c_z$  are the multiplicative and additive correction, respectively. We treat the multiplicative bias in the same way as the “free  $m$  correlated” model of A20, using the same mean and covariance matrix for the Gaussian prior (see Table I). Each redshift bin is corrected by

a multiplicative bias term that is drawn from a Gaussian distribution and the terms of the different bins are fully correlated. It was shown in A20 that treating the multiplicative biases as correlated or uncorrelated does not significantly affect the resulting constraints. We marginalize over this uncertainty by correcting each of the generated mock surveys (see section IV B) with a randomly drawn bias term after the mode removal (see section IV D and Figure 2).

We also treat the additive shear biases for each redshift bin. We remove the mean shear from all shear maps, simulated and observed alike, and then model the remaining uncertainty similar to the treatment of the real space correlation function  $\xi_+$  in A20. The mode removal (see section IV D) removes all B-modes from the shear maps and hence removes any additive correction from the imaginary part of the shear maps. Therefore, we only need to model the additive correction of the real part. We expect this correction to have a negligible impact on the results. Nevertheless, we use the same uncertainty  $\delta_c$  to model this additive correction as A20 used for their treatment of the correction in their  $\xi_1$  analysis. This correction is applied to each simulated survey after the mode removal (see section IV D and Figure 2).

### 3. Intrinsic Alignment

The intrinsic alignment of galaxies around massive objects is one of the most important systematic effects in weak gravitational lensing. We use the same model as in F19 which is based on the non-linear intrinsic alignment model (NLA) [35–37]. We refer the reader to F19 and [23] for details about the concrete implementation. Similar to F19 and A20, we ignore the redshift and luminosity dependence of the NLA model and only consider the intrinsic alignment amplitude  $A_{IA}$  as a free parameter. We create an intrinsic alignment map along each mock survey containing the cosmological signal. This intrinsic alignment map, scaled by the amplitude  $A_{IA}$ , can then be added to the actual signal map (see Figure 2). We also check the accuracy of our IA only maps by comparing their power spectra to PYCCL predictions. This comparison is presented in appendix B.

To constrain the intrinsic alignment amplitude, we extend the Sobol sequence of the grid cosmologies by an additional dimension and scale it to our prior on  $A_{IA}$  (see Table I). This way, each simulated cosmology has a unique amplitude which can be used for the parameter inference (see section IV H).

### 4. Baryonic Feedback

Baryonic effects can have a significant impact on the small scale clustering in large cosmological simulations [see e.g. 63–65]. However, modeling these effects is a challenging task as they depend on hydrodynamical interactions

which include sub-grid stellar and active galactic nuclei (AGN) feedback phenomena. In A20 these corrections are modelled at the level of the matter power spectrum by using the HMCODE [66]. The HMCODE introduces the baryonic feedback parameter  $A_{\text{bary}}$  that controls the strength of the corrections, with  $A_{\text{bary}} = 3.13$  corresponding to the dark-matter only case. Such a model is, however, not applicable for our map-based analysis. A possible way to introduce baryonic feedback into our simulations would be to run large-scale hydrodynamic simulations. However, these simulations are computationally very expensive, which is why multiple approaches to incorporate baryonic feedback into dark-matter-only simulations have been proposed [38, 67–69]. For example, [67] applied a deep learning based approach to directly “paint” baryonic feedback onto weak lensing maps. In this work we use a modified version of the *baryonification model* of [38–40] to incorporate baryonic feedback into our simulations. A different modified version of this method has already been used by [70] to perform a neural network analysis of flat weak lensing maps, showing that neural networks are capable to learn the relevant model parameters. The method works by adjusting the particle positions of dark-matter-only simulations such that the resulting density field includes the effects of gas and stars at cosmological scales. It has been shown by [39] that the corrected density field is in good agreement with full hydrodynamical simulations. We will only cover the most relevant aspects of the baryonification model here, and provide more details and benchmarks in appendix C. We refer the interested reader to [39] for a detailed description of the original model.

The baryonification model of [39] works by displacing  $N$ -body particles around dark matter halos, such that the resulting profiles include effects from stars and gas that are influenced by feedback processes. The original model has several free parameters that control the various effects. In our model we only vary the parameter  $M_c$  which dictates the mass dependence of the gas profile and has been shown to be the most important parameter for cosmology [71]. In contrast to the original model of [39], we do not directly use  $M_c$  as a baryonic parameter, but we instead assume

$$M_c = M_c^0 (1+z)^\nu, \quad (5)$$

where  $M_c^0$  and  $\nu$  correspond to our new model parameters. Equation (5) corresponds to an extension of the model in [39], allowing for an additional redshift dependence of the baryonic feedback effects. We fix the remaining parameters of the baryonification model to the best-guess parameters (model B-avrg), which can be found in table 2 of [39]. The values of the fixed parameters are motivated by observed X-ray gas fractions [72–74] including current uncertainties of the hydrostatic mass bias [75]. The fiducial values and priors of the two varying parameters ( $M_c^0, \nu$ ) are listed in table I.

In the original model, the particles are moved inside snapshots at a fixed redshift. However, the simulations

of the COSMOGRID were run in lighcone mode, meaning that we only have access to the particle shells instead of full snapshots. Therefore, we use the friends-of-friends (FoF) halo catalogue of the COSMOGRID simulations to adapt the particle shells instead of the positions of individual particles inside snapshots. We provide more details about this procedure in appendix C. Similar to the treatment of the intrinsic alignment amplitude, we extent the Sobol sequence of the grid cosmologies by two dimension to assign each simulated cosmology a unique set of parameters ( $M_c^0, \nu$ ). We then generate a second set of simulated shells that contain the baryonic corrections for all simulations. For the fiducial simulations, their perturbations and the benchmarks, we chose our fiducial baryon correction parameters and their corresponding perturbations according to table I. One should note that the fiducial baryon correction parameters are not equivalent to the dark-matter-only case, but reflect the best-guess parameters of [39]. Using this second set of shells, we repeat the previously described procedure to generate mock surveys. This allows us to perform an analysis that fully incorporates baryonic effects at the level of the model described above.

### 5. Simulation Settings

The results of the analysis should be robust with respect to the simulation settings. We check this robustness using mock observations of the benchmark simulations (see section IV A 3). In this way we can test the influence of the number of particles, the box size, and the redshift resolution of the shells on the cosmological constraints. The number of particles is relevant for the resolution at small scales. Using a larger box size enables us to measure the impact of potential super survey modes. Finally, the benchmark with the higher redshift resolution makes it possible to check if the number of base time steps of the simulations is sufficiently large. The results of these tests are presented in section V.

### F. Graph Convolutional Neural Network

Due to the large survey area and footprint of the KiDS-1000 data, the curvature of the sky needs to be taken into account. In F19, this problem was solved by projecting parts of the survey onto flat patches. However, in this work, we choose to treat the survey as a whole. There are multiple approaches to deal with data on the sphere in machine learning. Following [28] we chose to use DEEPSPIRE [76], described in [41], which treats the pixel of the maps as nodes in a graph. DEEPSPIRE has two main types of layers that are described in [28, 41]. First, pseudo convolutions make use of the HEALPix pixelization and are used to reduce the  $n_{\text{side}}$  of the maps with trainable weights. These layers can only be applied if the input maps are padded correctly (see [28]). This

TABLE II. Fiducial architecture of the used GCNN. We report layer type, output shape ( $N_b$  being the batch size) and number of trainable parameters. The residual layer (see Figure 5 of [28]) is repeated five times. The output of the network is only four dimensional since we decided to ignore certain parameters in the loss (see section IV F 1).

Layer Type	Output Shape	# Parameter
Input	$(N_b, 149504, 10)$	0
Pseudo Convolution	$(N_b, 37376, 32)$	1312
Pseudo Convolution	$(N_b, 9344, 64)$	8256
Pseudo Convolution	$(N_b, 2336, 128)$	32896
Chebyshev Convolution	$(N_b, 2336, 256)$	163840
Layer-Normalization	$(N_b, 2336, 256)$	512
Pseudo Convolution	$(N_b, 584, 256)$	262400
Chebyshev Convolution	$(N_b, 584, 256)$	327680
Layer-Normalization	$(N_b, 584, 256)$	512
Pseudo Convolution	$(N_b, 146, 256)$	262400
Residual Layer	$(N_b, 146, 256)$	656896
	$\vdots$	
Residual Layer	$(N_b, 1672, 128)$	170528
Flatten	$(N_b, 37376)$	0
Layer-Normalization	$(N_b, 37376)$	74752
Fully Connected	$(N_b, 4)$	149508

padding, visualized in Figure 1, is necessary such that the lower resolution maps have a valid number of pixels. The other type of layers are graph convolutions, which are expressed in terms of Chebyshev polynomials and applied to the data via the graph Laplacian. These layers can be used to construct composite layers like residual layers. In this work we use the same settings and types of layers as in [28]. Our fiducial architecture is listed in table II. All layers of networks used in this work, if not mentioned otherwise, use the linear rectified unit (ReLU) as activation function. We trained a total of three networks with the same fiducial architecture (see section IV F 1). Additionally, we trained three similar networks to check the robustness of the results regarding certain choices of hyperparameters. The first network was trained with a larger batch size (see section IV F 1). The second was trained with more residual layers and the third one was trained without graph convolutional layers. These networks are described in more detail in appendix D, and we will refer to them as “benchmark networks”.

#### 1. Training

We used both shear components of all five redshift bins as the input of the graph convolutional neural network (GCNN), resulting in a total of ten input channels (see table II). We trained the GCNNs using the fiducial simulations of the COSMOGRID and the information maximizing loss presented in [28] that is based on [42] and optimizes the Cramér-Rao bound. The loss function is given by

$$L = \log \det(\text{Cov}_\theta(\hat{s})) - 2 \log \left| \det \left( \frac{\partial \Psi_\theta(\hat{s})}{\partial \theta} \right) \right|, \quad (6)$$



where  $\hat{s}$  is the output of the network (summary), and  $\Psi_\theta(\hat{s})$  is the expected value of  $\hat{s}$  for input maps that were generated with the cosmological and nuisance parameters  $\theta$ . We found that using all parameters leads to instabilities during the training because the signal originating from some parameters is fairly weak. We therefore decided to only use the four parameters for the training to which weak lensing is most sensitive to  $\theta = (\Omega_M, \sigma_8, w_0, A_{\text{IA}})$ . One should note that this does not correspond to a marginalization of the remaining parameters. The network will still output different results if for example  $\Omega_b$  is changed. However, the network is not aware of the missing parameters during the training. Additionally, to make the training more stable we used the regularizer proposed in [28]

$$L_{\text{regu}} = \lambda \left\| \frac{\partial \Psi_\theta(\hat{s})}{\partial \theta} - \mathbf{I} \right\|, \quad (7)$$

where we set  $\lambda = 100$  and  $\mathbf{I}$  is the identity matrix. The training is performed on the mock surveys without baryon corrections. We found that simply evaluating the normally trained network on the mock surveys containing baryon corrections leads to similar results as retraining the network with the new maps. The reason for this is most likely the high noise level of the maps and the low signal originating from the baryon nuisance parameters. The covariance  $\text{Cov}_\theta(\hat{s})$  is estimated empirically during the training and the derivatives of the expected value are calculated empirically and with a finite difference method using the fiducial simulations with perturbed parameters (see table I). Each network, fiducial architecture or benchmark, is trained for 100'000 steps on eight GPUs in a data-parallel fashion on the supercomputer Piz Daint [77]. Each GPU had a local batch size of eight, leading to a final batch size of 64, with the exception of the benchmark model that used a larger total batch size (see appendix D), which was trained on 16 GPUs. The weight optimization is done using the Adam optimizer [78] with an initial learning rate of 0.0001 and moments  $\beta_1 = 0.9$  and  $\beta_2 = 0.999$ . As in [28], we clip the gradient, reducing the global norm to 5.0 if necessary to avoid large weight updates. One should note that the actual input of the network is a batch of 576 because of the perturbed maps that have to be evaluated to estimate the derivative used in the loss (see equation (6)). During every training step each fiducial map in the current batch is augmented with random multiplicative and additive shear biases and paired with a random noise realization. We observed that the networks are overfitting by learning the 16'000 noise maps of our fiducial set, if we trained the networks for long enough. This overfitting could potentially be avoided by using more regularization techniques like dropout [79]. We leave such applications to future work. To mitigate the overfitting during the inference, we use new noise realizations (see section IV C) for the evaluation. We evaluate the whole dataset, fiducial and grid, every 10'000 steps.

TABLE III. Architecture of the used summary networks. We report layer type, output shape ( $N_b$  being the batch size) and number of trainable parameters. The fully connected layers in the middle are repeated nine times. The output of the network is only four dimensional since we decided to ignore certain parameters in the loss (see section IV G 1)

Layer Type	Output Shape	# Parameter
Input	$(N_b, 450)$	0
Layer-Normalization	$(N_b, 450)$	900
Fully Connected	$(N_b, 512)$	230912
Fully Connected	$(N_b, 256)$	131328
Fully Connected	$(N_b, 256)$	65792
	$\vdots$	
Fully Connected	$(N_b, 256)$	65792
Fully Connected	$(N_b, 3)$	1028

## G. Summary Networks

Additionally to the GCNN, we train standard fully connected networks on pre-calculated summary statistics. To train the network we evaluate the summary statistics of 128'000 combinations of signal and noise maps for the fiducial simulations and perturbations using only the noise generated for the training. We also evaluate the summary statistics using the maps of the grid cosmologies and the evaluation set of the fiducial simulations. For each generated survey we evaluate the auto- and cross-spectra in 30 linearly spaced bins for  $\ell \in [0, 1500]$ , covering almost all resolvable scales. Further, we perform a peak count analysis with auto- and cross-peaks similar to [10]. However, we found that including the peak counts in the input of the networks did not significantly increase the performance. This is most likely because of the low resolution of the maps and the small survey area, making it hard for peak counts to extract a strong signal. Therefore, we did not use any additional summaries besides the auto- and cross-correlations. The architecture of the networks is presented in table III.

### 1. Training

We train three instances of the summary networks presented in table III for 100'000 steps using the same optimizer settings and gradient clipping as for the GCNN. However, since the input data is significantly smaller, we could perform the training on a single GPU with a batch size of 1'024. As for the GCNN we reduce the relevant parameters for the training to  $\theta = (\Omega_M, \sigma_8, w_0, A_{\text{IA}})$ . The input of the network is the logarithm of the absolute value of the auto- and cross-spectra. This transformation is performed to avoid the usually very small values of the spectra. Training the network this way can lead to significant overfitting, as only 128'000 different samples are available. Therefore, we added a standard L2 regularization term with a weight of 0.25 to the loss. Again, we

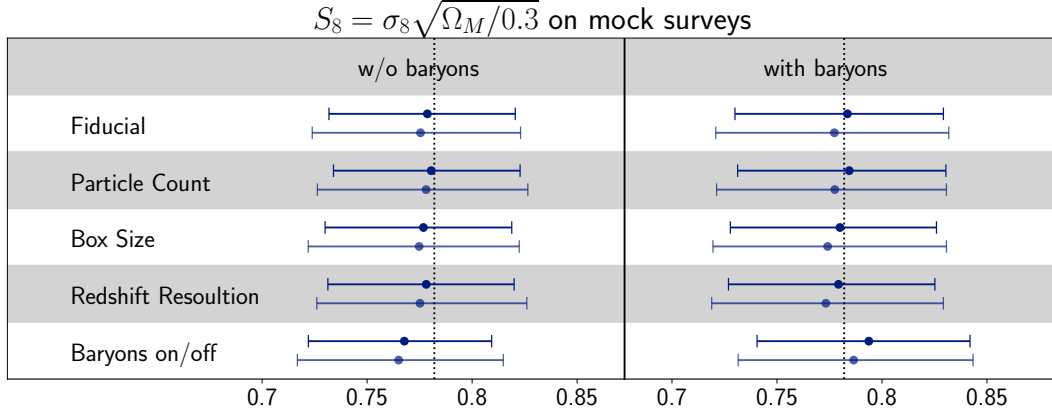


FIG. 5. Constraints of the degeneracy parameter  $S_8$  using mock observations generated from the COSMOGRID benchmark simulations. The error bars correspond to the 68% confidence intervals and the dots indicate the expected value. The upper constraints on each stripe were generated using the GCNNs and summary networks while the lower ones stem from our power spectra analysis. The left column of the plot shows the constraints without including Baryonic corrections in the simulated maps used for the inference, i.e. the maps used for the evaluation of the GNCC and power spectra, while the constraints in the right column includes them. Besides the last row, the mock observations used in the left column also ignore Baryon feedback. The last row shows the constraints for the fiducial mock observation (first row) again, but including Baryonic correction in the left column and ignoring them in the right column.

evaluate the whole evaluation dataset, fiducial and grid, every 10'000 steps.

## H. Parameter Inference

We perform the parameter inference in the same way as [28], by using Gaussian Process Approximate Bayesian Computation (GPABC). We estimate the ABC log-posterior of a grid point  $\theta$  by using the summaries of the  $n_x = 280$  mock surveys via

$$\hat{\mathcal{L}}(\theta) = \log \left( \frac{p(\theta)}{n_x} \sum_{i=1}^{n_x} K_h(\|\hat{s}_i - \hat{s}_{\text{obs}}\|_M) \right), \quad (8)$$

where  $p(\theta)$  is the (flat) prior,  $K_h$  is a kernel with scale  $h$  and  $\|\cdot\|_M$  represents the Mahalanobis distance using the fiducial covariance matrix

$$\|y\|_M^2 = y^T \text{Cov}_\theta(\hat{s})^{-1} y. \quad (9)$$

Additionally, the variance of this estimate can be obtained via

$$\sigma^2(\theta) = \frac{p(\theta)^2}{n_x} \frac{\text{Var}[K_h(\|\hat{s}_i - \hat{s}_{\text{obs}}\|_M)]}{\hat{p}_{\text{ABC}}(\theta|\hat{s}_{\text{obs}})}, \quad (10)$$

where the ABC posterior is defined via

$$\hat{\mathcal{L}}(\theta) = \log(\hat{p}_{\text{ABC}}(\theta|\hat{s}_{\text{obs}})). \quad (11)$$

In this work, we exclusively use the sigmoid kernel

$$K_h(x) = \frac{2}{\pi h} \frac{1}{\exp\left(\frac{x}{h}\right) + \exp\left(-\frac{x}{h}\right)}. \quad (12)$$

The scale  $h$  is a hyperparameter and generally depends on the observation. These log-posterior estimates along with their uncertainty can then be interpolated using Gaussian process (GP) regression. The GP can then be evaluated to obtain confidence intervals for the model parameters with standard techniques like Markov Chain Monte Carlo (MCMC). In this work, we use the `emcee` algorithm described in [80] with 1'024 walkers each sampling 5'000 samples. With these settings, sampling the emulated posterior takes roughly three minutes on a single GPU on Piz Daint.

### 1. Power Spectra Analysis

To check the consistency of our network analysis, we first perform a power spectrum analysis using a standard compression scheme. The compression is necessary as the ABC log-posterior estimates generally become less noisy if the summary vector has fewer dimensions, which is known as the curse of dimensionality. The dimensional reduction is performed using the standard MOPED compression [82]. The MOPED algorithm performs a linear transformation that aims to preserve as much information about the relevant model parameter as possible. Given any summary  $\hat{s}$ , the  $i$ -th entry of the compressed vectors is obtained via

$$\hat{y}_i = b_i^T \hat{s}, \quad (13)$$

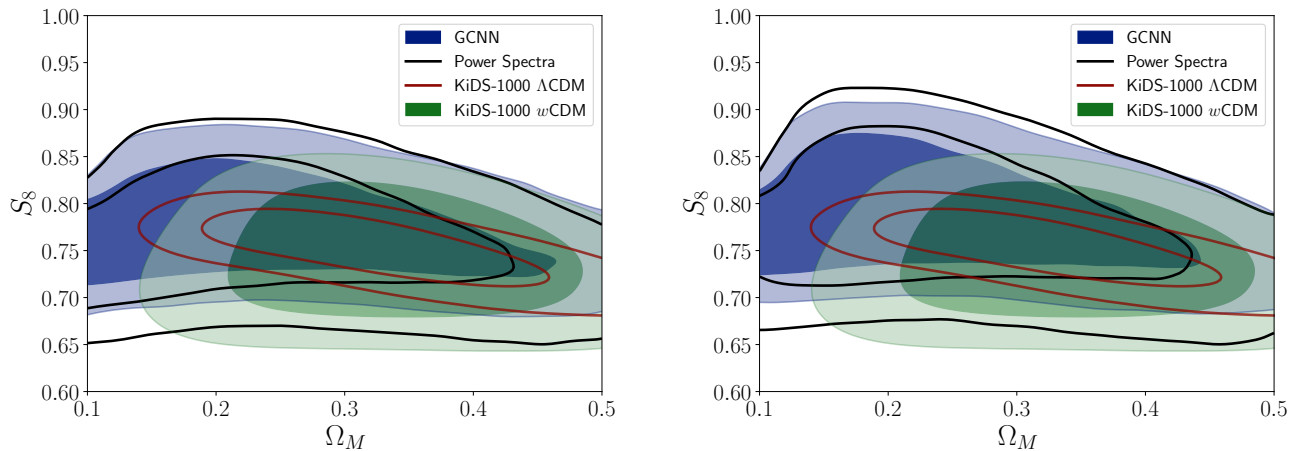


FIG. 6. The fiducial results of our analysis compared to the band power constraints of F19 and the KiDS-1000  $w$ CDM analysis [81]. The left plot shows the results without the treatment of baryons, while the right plot includes baryonic feedback.

where the linear transformation is defined via

$$b_i = \frac{\text{Cov}_\theta(\hat{s})^{-1} \frac{\partial \Psi_\theta(\hat{s})}{\partial \theta_i} - \sum_{q=1}^{i-1} \left( \frac{\partial \Psi_\theta(\hat{s})}{\partial \theta_i}^T b_q \right) b_q}{\sqrt{\frac{\partial \Psi_\theta(\hat{s})}{\partial \theta_i} \text{Cov}_\theta(\hat{s})^{-1} \frac{\partial \Psi_\theta(\hat{s})}{\partial \theta_i} - \sum_{q=1}^{i-1} \left( \frac{\partial \Psi_\theta(\hat{s})}{\partial \theta_i}^T b_q \right)^2}}. \quad (14)$$

We compress the auto- and cross-correlation of all mock surveys using the compression matrix generated with the auto- and cross-spectra of the fiducial simulations and their perturbations. The output vector  $\hat{y}$  contains one entry for each model parameter, which is seven for mock surveys without baryonic corrections and nine if baryonic corrections are included. The compressed vectors can then be used for parameter inference with GPABC.

## 2. Network Analysis

Similar to F19, we decided to combine multiple networks to improve the results. We therefore use all predictions from all fiducial GCNN and summary networks. All networks were evaluated every 10'000 training steps, meaning that the output of a single network for a single mock observation is 40 dimensional (four outputs  $\times$  ten evaluations). All six networks combined would therefore have an output dimension of 240. This high dimensionality would deteriorate the performance of the GPABC significantly. In [28] it was therefore proposed to perform as a second compression using a fully connected network and the previously introduced information maximizing loss (see equation (6)). However, at this point, we only have access to 16'000 evaluations of the fiducial mock surveys to optimize the weights of the networks. This low number might lead to severe overfitting in the optimization. Therefore, we decided to use the standard MOPED compression instead. To perform a MOPED compression, one has to calculate the inverse

of the covariance matrix of the fiducial predictions (see equation (14)). This inversion can be numerically unstable if the covariance matrix is not well conditioned, e.g. because the vectors are very correlated. To avoid this instability, we performed a MOPED compression for all predictions of the GCNN and summary networks individually. This reduced the dimensionality of the outputs from the three GCNN and summary networks from 120 to the four, one for each parameter that we trained the networks on (see sections IV F 1 and IV G 1). Afterward, we took the mean of the two compressed vectors as the final summary. Theoretically, it would be better to perform a single MOPED compression on the full 240 dimensional output, as it would also consider the correlations between the predictions of the GCNNs and summary networks. However, we found that the numerical instability caused by the ill-conditioned matrix actually degrades the performance. This could be solved by increasing the number of fiducial mock surveys, which we will leave to future work.

All results of our network analysis presented in the main paper use this combination of six networks. We present some constraints with different settings, including constraints from our benchmark networks, in appendix D.

## V. TESTS ON MOCK OBSERVATIONS

In this section we present cosmological constraints that are generated with mock observations from the COSMO-GRID benchmark simulations. These tests are performed for three reasons. First, to check if our power spectrum analysis is consistent with the network analysis. Second, to see if our pipeline can correctly recover the input parameters of the mock observations. And third, to examine the effects of the different simulation settings (including baryonic feedback effects) on the constraints. The inference is done as explained in section IV H with the scale

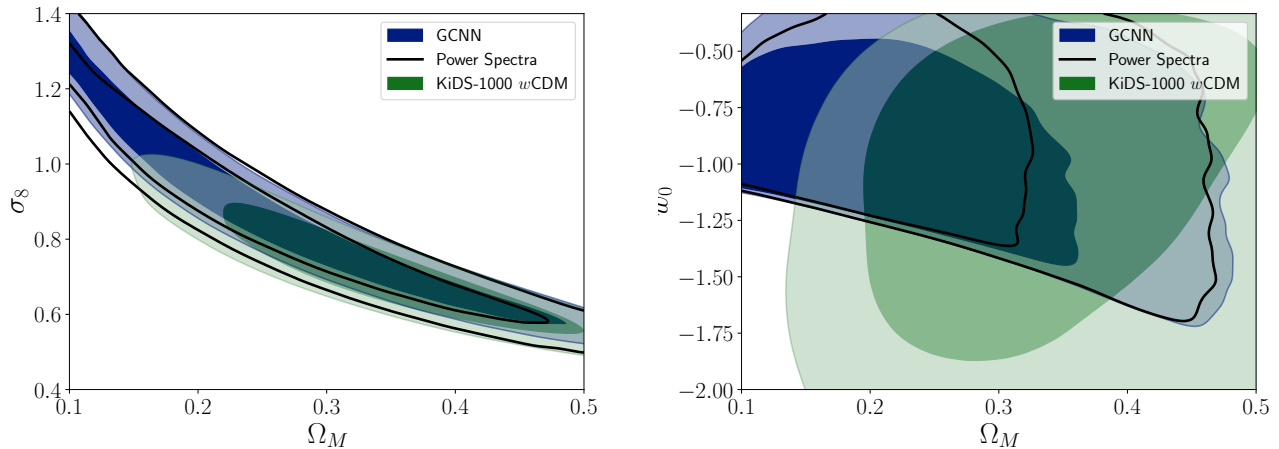


FIG. 7. The fiducial constraints of our analysis including baryon feedback compared to the KiDS-1000  $w$ CDM analysis [81]. The left plot shows the degeneracy of the  $\Omega_M - \sigma_8$  plane, while the right plot shows the constraints of the dark energy equation of state parameter  $w_0$ . The lower bound of  $w_0$  of our constraints purely dominated by our prior (see appendix A).

parameter set to  $h = 0.4$ . As mock observations, we choose the mean predictions of all 400 mock surveys from the COSMOGRID benchmark simulations. We choose the mean predictions to decrease the spread of the cosmic variance. We present the 68% confidence regions and mean predictions of the degeneracy parameter

$$S_8 \equiv \sigma_8 \sqrt{\frac{\Omega_M}{0.3}} \quad (15)$$

in Figure 5. It can be seen that all constraints are consistent with each other and also with the input parameter. The impact of the different simulation settings is small and similar to the findings of F19. However, the impact of the baryonic corrections is significantly smaller. This can be seen in the last row of the plot, where we use the fiducial mock observation including Baryonic feedback in the analysis that ignores Baryons or ignore Baryonic feedback in the analysis that uses the baryonic correction model respectively. The smaller impact is mainly caused by the chosen scale cuts. The resolution of the maps in F19 is much higher, leading to more non-Gaussian information, but also increasing the impact of baryonic physics. The scale cuts in this work ( $\ell_{\max} \sim 1500$ ) are similar to the ones in A20 and the measured shifts caused by either including the baryonic corrections in the mock observation, but not in the data or vice versa are consistent with the findings in A20. This shows that the implemented baryonification model is consistent with the HMCODE implementation used in A20, at least at the level of the cosmological constraints. Generally, including baryonic feedback into the analysis increases the confidence intervals by  $\sim 10\%$ , which is expected.

Another important difference to the results of F19 is that the constraints of the networks analysis are on average only  $\sim 10\%$  tighter than the constraints of the power spectrum analysis, as opposed to the  $\sim 30\%$  improve-

ment reported in F19. There are multiple reasons for this difference. The most important two being the different scale cuts and the choice of the scale parameter  $h$  in the GPABC. The high resolution maps used in F19 include much more non-Gaussian information, increasing the performance of the networks. We expected the gain of the networks to drop, considering the low resolution maps used in this analysis. Further, all constraints generated with GPABC require the choice of the scale parameter  $h$ . This parameter acts like a smoothing scale on the constraints and makes it possible to obtain constraints even if the simulated grid is very coarse. Increasing  $h$  leads to broader constraints, but the expected value remains largely unchanged. Theoretically, one should optimize  $h$  for all constraints individually. However, since here, we are only interested in the consistency of the constraints as opposed to the actual size, we chose a fairly conservative  $h = 0.4$  for all constraints. We decided to only optimize  $h$  for the final constraints after the unblinding (see sections III and VI).

All constraints presented in this section are generated using the fiducial setting described in section IV H. Further tests can be found in appendix D.

## VI. RESULTS

As mentioned in section III, we unblinded our results after making sure that our pipeline successfully recovers the parameters of the mock observations, that the results of the network and power spectra analysis are consistent, and that the pipeline is robust against simulation settings. Our fiducial constraints are presented in Figure 6. The results were generated in the same way as the constraints in section V and generally consistent with the results of A20 and the KiDS-1000  $w$ CDM analysis [81]. The results



including the baryon corrections prefer a slightly higher value of the degeneracy parameter  $S_8$ . This is consistent with our checks from section V. A comparison of  $S_8$  constraints of various settings and external analyses is shown in Figure 9. We show the same constraints in the  $\Omega_M - \sigma_8$  and  $\Omega_M - w_0$  planes in Figure 7. Additionally, we present the full parameter constraints in appendix E. We constrain the degeneracy parameter to  $S_8 = 0.76^{+0.05}_{-0.05}$  with our power spectrum analysis ignoring including baryon feedback and to  $S_8 = 0.78^{+0.06}_{-0.06}$  if we include our baryon treatment. Including the baryon correction increases the constraints by 14%, which is roughly consistent with the findings of A20 and our tests on mock observations. Our fiducial analysis with the GCNN constrains the degeneracy parameter to  $S_8 = 0.77^{+0.04}_{-0.05}$  when ignoring baryon corrections and to  $S_8 = 0.79^{+0.05}_{-0.05}$  when including baryon feedback. This is an 14% and 16% improvement respectively when compared to our power spectrum analysis, which is also consistent with our tests on mock observations. Both, our power spectrum and GCNN analysis, show the typical degeneracy in the  $\Omega_M - \sigma_8$  plane, which is shown in Figure 7. Our constraints on the dark energy equation of state parameter are mostly dominated by our prior and consistent with the  $\Lambda$ CDM model. However, our fiducial GCNN analysis is able to put an upper bound on  $w_0 = -0.93^{+0.32}_{-0.29}$  at the 68% confidence level, while the lower bound is determined by our prior distribution. Finally, we are also able to constrain the intrinsic alignment amplitude. The fiducial results of our power spectrum analysis constrain the intrinsic alignment amplitude to  $A_{IA} = 0.77^{+0.86}_{-0.70}$  without baryon corrections and to  $A_{IA} = 0.73^{+0.88}_{-0.70}$  when including baryons. The GCNN analysis yields the constraints  $A_{IA} = 0.51^{+0.67}_{-0.66}$  and  $A_{IA} = 0.46^{+0.67}_{-0.67}$ , respectively, leading to an improvement of  $\sim 15\%$ . These constraints are consistent with

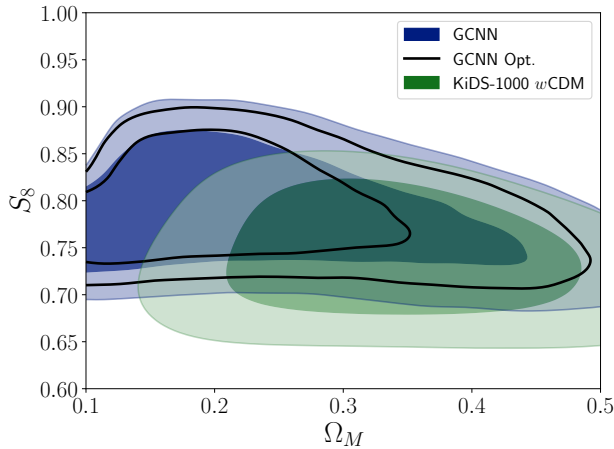


FIG. 8. The fiducial GCNN constraints of this work compared to the optimized version that was obtained by reducing the scale parameter of the GPABC.

the GCNN analysis having the tendency to prefer slightly lower intrinsic alignment amplitudes as the power spectrum analysis.

In Figure 8, we show the constraints of our GCNN analysis, where we decreased the smoothing scale of the GPABC to  $h = 0.2$ , which we dub “GCNN optimized”. As mentioned in section V, the smoothing scale of the GPABC is a hyperparameter that can be optimized for each observation. For our fiducial constraints, we chose the same, conservative scale  $h = 0.4$  as for our tests on mock observations. Decreasing this parameter can lead to tighter constraints, however, choosing a value that is too small will lead to a noisy posterior similar to choosing a threshold that is too small in a standard rejection ABC analysis. A demonstration of the impact of the smoothing parameter is given in the appendix of [28]. Our results are generally robust to small changes to this parameter, indicating that the parameter choice did not lead to a noisy posterior. Decreasing it further only leads to marginal improvements of the constraints. Using this new scale, the constraints of the degeneracy parameter improve to  $S_8 = 0.78^{+0.04}_{-0.04}$  without the treatment of baryons and to  $S_8 = 0.79^{+0.04}_{-0.05}$  if baryon corrections are included. This corresponds to a  $\sim 11\%$  improvement when compared to the fiducial GCNN results.

Our results are also consistent with the results of A20 and the KiDS-1000  $w$ CDM analysis [81]. Our analysis results in slightly higher values for the degeneracy parameter  $S_8$ , but the difference is less than one standard deviation. The  $S_8$  constraints of our fiducial power spectrum analysis including baryon corrections are 18% larger than the results of the KiDS-1000  $w$ CDM analysis [81]. Looking at Figures 9 and 7, one can see that the difference is mostly coming from the low  $\Omega_M$  regime that the KiDS-1000  $w$ CDM analysis is able to exclude as compared to our analysis. These differences are most likely caused by the different modeling choices. The KiDS-1000  $w$ CDM analysis and our power spectrum analysis are fairly similar, however, there are some important differences. The most important being the different weighing schemes of the  $\ell$ -modes, the baryon treatment, and the different prior choices. While the scale cuts are comparable, it is worth noting that our map-based approach with a resolution of  $n_{\text{side}} = 512$  significantly down-weights the high  $\ell$ -modes because of the pixel window function. Furthermore, as we described in section IV E 4, the baryon treatment is based on two entirely different methods. And lastly, the KiDS-1000  $w$ CDM analysis has a flat prior in  $\omega_{\text{cdm}} \equiv \Omega_{\text{cdm}} h^2$  and  $\omega_b \equiv \Omega_b h^2$  which does not translate into a flat prior in  $\Omega_M$  and  $\Omega_b$  that our analysis is using. These modeling differences can potentially explain the differences in the results.

Our fiducial  $S_8$  constraints including baryon correction of the GCNN analysis have the same size as the constraints of the KiDS-1000  $w$ CDM analysis [81], but are  $\sim 1\sigma$  higher, while our optimized results are 11% smaller. Due to the preference of higher  $S_8$ -values in our analysis, we find a lower tension with the results of Planck [83]. Our

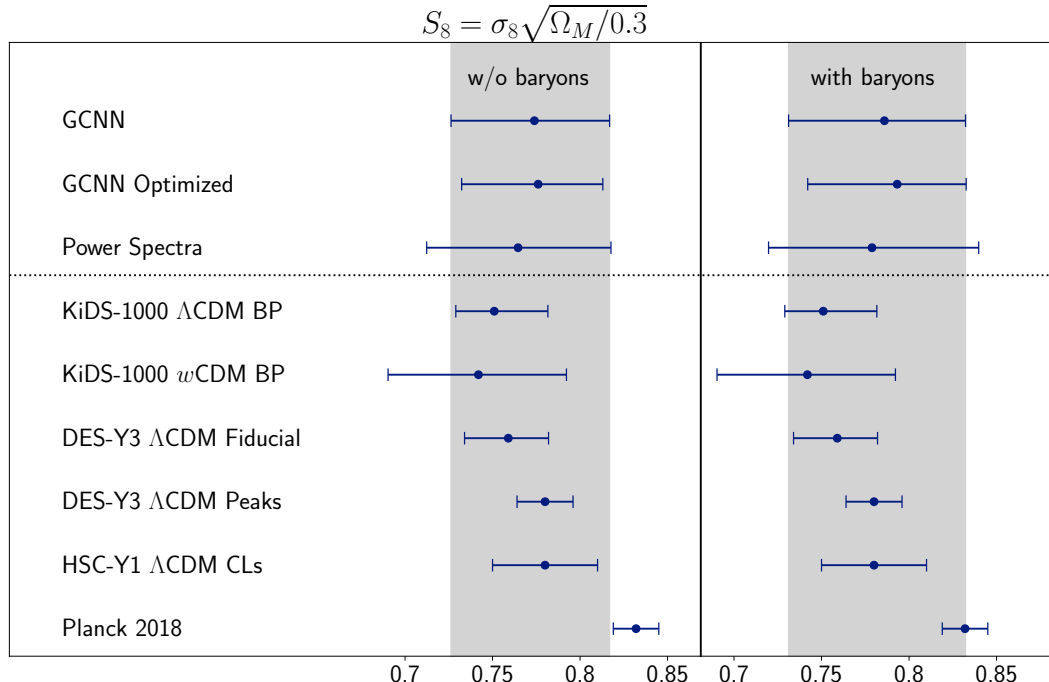


FIG. 9. A comparison of our constraints of the degeneracy parameter  $S_8$  with different external analyses. The first three results are from this work, where the left column shows our results without the treatment of baryon correction and the results in the right column include baryon corrections. We compare our results to the band power constraints of A20, the KiDS-1000  $w$ CDM analysis [81], the fiducial DES-Y3 results [9], the DES-Y3 peaks analysis [10], the HSC-Y1 results [12] and the Planck 2018 (TT,TE,EE + lowE + lensing) [83] constraints.

constraints of the intrinsic alignment amplitude are generally consistent with the results from A20 and KiDS-1000  $w$ CDM analysis [81], with a tendency towards slightly smaller values.

## VII. CONCLUSION

In this work, we presented a fully forward-modeled  $w$ CDM analysis of the KiDS-1000 data that is consistent with previous results and shows the potential of neural networks in cosmological parameter inference. We used the simulations of the COSMOGRID to generate almost one million mock surveys of the KiDS-1000 data, including the treatment of systematic effects like the photometric redshift bias or the multiplicative and additive shear biases. Additionally, we treat the effect of intrinsic galaxy alignment and baryon corrections on map level to incorporate them into our analysis. We then performed a standard power spectrum analysis and we trained GCNNs using DEEPSPHERE with an information maximizing loss. Finally, we applied the method described in [28] to perform a likelihood-free cosmological parameter inference.

Our results of the power spectrum and network analysis

are generally consistent with each other and also with the results from A20 and the KiDS-1000  $w$ CDM analysis [81]. We find a preference for slightly higher  $S_8$  values which can potentially be explained by the different modeling choices. Similar to the results of F19 we find that the networks generally perform better than the power spectrum analysis, leading to  $\sim 15\%$  smaller constraints in  $S_8$  and  $A_{IA}$ , with our GCNN analysis giving similar constraints as the KiDS-1000  $w$ CDM analysis [81]. Optimizing the hyperparameter of the GPABC leads to a further decrease of the  $S_8$  constraints by  $\sim 11\%$ .

Including baryon corrections into our analysis generally broadens the constraints by  $\sim 10\%$ , affecting the network and power spectrum analysis to a similar degree. Additionally, we find that including baryons into the analysis leads to slightly higher values of  $S_8$ , which agrees with the results of A20, showing that the implemented baryon model is consistent with other treatments at the level of the cosmological parameter constraints.

Potential extensions of this work include a more advanced intrinsic alignment model, less conservative scale cuts and the analysis of other surveys such as the dark energy survey (DES). We believe that using a finer resolution of the mock surveys will, most likely, greatly improve the

performance of the networks, similar to gains presented in F19. A finer resolution of the mock surveys would require additional tests of the simulations and the baryon model. At the same time it would also drastically increase the storage requirements along with the computational resources necessary to analyse the data. For example, increasing the resolution to a HEALPix  $n_{\text{side}} = 1024$  would increase the storage necessary for the mock surveys by a factor of four and similarly affect the training times of the networks. However, larger data sets might also be able to reduce the prior ranges of the cosmological parameters, reducing the necessary number of simulations of the COSMOGRID. Overall this offers great prospects for machine learning inference for current and weak lensing surveys.

## ACKNOWLEDGMENTS

JF would like to thank Jeppe Mosgaard Dakin for helpful discussions and especially his contribution to the

$w_0 - \Omega_M$  prior of the simulation grid. We thank Joachim Stadel and Douglas Potter for helpful discussions.

This work was supported by a grant from the Swiss National Supercomputing Centre (CSCS) under project ID s998, entitled “Measuring dark energy with deep learning”.

We would like to thank the technical support teams of the Euler and Piz Daint computing clusters.

AS acknowledges support from the Swiss National Science Foundation via the grant PCEFP2.181157.

This work is based on observations made with ESO Telescopes at the La Silla Paranal Observatory under programme IDs 177.A-3016, 177.A-3017, 177.A-3018 and 179.A-2004, and on data products produced by the KiDS consortium. The KiDS production team acknowledges support from: Deutsche Forschungsgemeinschaft, ERC, NOVA and NWO-M grants; Target; the University of Padova, and the University Federico II (Naples).

- 
- [1] P. Schneider, “Weak Gravitational Lensing,” *arXiv e-prints*, pp. astro-ph/0509252, Sep 2005.
  - [2] M. Kilbinger, “Cosmology with cosmic shear observations: a review,” *Reports on Progress in Physics*, vol. 78, p. 086901, Jul 2015.
  - [3] [cfhtlens.org](http://cfhtlens.org).
  - [4] E. Grocutt, F. Simpson, C. Heymans, *et al.*, “CFHTLenS tomographic weak lensing cosmological parameter constraints: Mitigating the impact of intrinsic galaxy alignments,” *Monthly Notices of the Royal Astronomical Society*, vol. 432, pp. 2433–2453, 05 2013.
  - [5] [kids.strw.leidenuniv.nl](http://kids.strw.leidenuniv.nl).
  - [6] H. Hildebrandt, F. Köhlinger, J. L. van den Busch, *et al.*, “KiDS+VIKING-450: Cosmic shear tomography with optical+infrared data,” *arXiv e-prints*, p. arXiv:1812.06076, Dec 2018.
  - [7] Asgari, Marika, Lin, Chieh-An, Joachimi, Benjamin, *et al.*, “Kids-1000 cosmology: Cosmic shear constraints and comparison between two point statistics,” *A&A*, vol. 645, p. A104, 2021.
  - [8] [darkenergysurvey.org](http://darkenergysurvey.org).
  - [9] L. F. Secco, S. Samuroff, E. Krause, *et al.*, “Dark Energy Survey Year 3 Results: Cosmology from Cosmic Shear and Robustness to Modeling Uncertainty,” *arXiv e-prints*, p. arXiv:2105.13544, May 2021.
  - [10] D. Zürcher, J. Fluri, R. Sgier, *et al.*, “Dark Energy Survey Year 3 results: Cosmology with peaks using an emulator approach,” *arXiv e-prints*, p. arXiv:2110.10135, Oct. 2021.
  - [11] [hsc.mtk.nao.ac.jp/ssp/survey](http://hsc.mtk.nao.ac.jp/ssp/survey).
  - [12] C. Hikage, M. Oguri, T. Hamana, *et al.*, “Cosmology from cosmic shear power spectra with Subaru Hyper Suprime-Cam first-year data,” *Publications of the Astronomical Society of Japan*, vol. 71, 03 2019. 43.
  - [13] R. Laureijs, J. Amiaux, S. Arduini, *et al.*, “Euclid Definition Study Report,” *arXiv e-prints*, p. arXiv:1110.3193, Oct 2011.
  - [14] C. Chang, M. Jarvis, B. Jain, *et al.*, “The effective number density of galaxies for weak lensing measurements in the LSST project,” *Monthly Notices of the Royal Astronomical Society*, vol. 434, pp. 2121–2135, Sep 2013.
  - [15] D. Spergel, N. Gehrels, C. Baltay, *et al.*, “Wide-Field Infrared Survey Telescope-Astrophysics Focused Telescope Assets WFIRST-AFTA 2015 Report,” *arXiv e-prints*, p. arXiv:1503.03757, Mar. 2015.
  - [16] J. Liu, A. Petri, Z. Haiman, *et al.*, “Cosmology constraints from the weak lensing peak counts and the power spectrum in cfhtlens data,” *Phys. Rev. D*, vol. 91, p. 063507, Mar 2015.
  - [17] J. P. Dietrich and J. Hartlap, “Cosmology with the shear-peak statistics,” *Monthly Notices of the Royal Astronomical Society*, vol. 402, pp. 1049–1058, Feb 2010.
  - [18] T. Kacprzak, D. Kirk, O. Friedrich, *et al.*, “Cosmology constraints from shear peak statistics in Dark Energy Survey Science Verification data,” *Monthly Notices of the Royal Astronomical Society*, vol. 463, pp. 3653–3673, Dec 2016.
  - [19] J. Fluri, T. Kacprzak, R. Sgier, *et al.*, “Weak lensing peak statistics in the era of large scale cosmological surveys,” *Journal of Cosmology and Astro-Particle Physics*, vol. 2018, p. 051, Oct 2018.
  - [20] X. Liu, C. Pan, R. Li, *et al.*, “Cosmological constraints from weak lensing peak statistics with Canada-France-Hawaii Telescope Stripe 82 Survey,” *Monthly Notices of the Royal Astronomical Society*, vol. 450, pp. 2888–2902, July 2015.
  - [21] H. Shan, X. Liu, H. Hildebrandt, *et al.*, “KiDS-450: cosmological constraints from weak lensing peak statistics - I. Inference from analytical prediction of high signal-to-noise ratio convergence peaks,” *Monthly Notices of the Royal Astronomical Society*, vol. 474, pp. 1116–1134, Feb 2018.
  - [22] N. Martinet, P. Schneider, H. Hildebrandt, *et al.*, “KiDS-450: cosmological constraints from weak-lensing peak

- statistics - II: Inference from shear peaks using N-body simulations,” *Monthly Notices of the Royal Astronomical Society*, vol. 474, pp. 712–730, Feb 2018.
- [23] D. Zürcher, J. Fluri, R. Sgier, *et al.*, “Cosmological forecast for non-gaussian statistics in large-scale weak lensing surveys,” *Journal of Cosmology and Astroparticle Physics*, vol. 2021, pp. 028–028, Jan 2021.
- [24] E. Semboloni, T. Schrabback, L. van Waerbeke, *et al.*, “Weak lensing from space: first cosmological constraints from three-point shear statistics,” *Monthly Notices of the Royal Astronomical Society*, vol. 410, pp. 143–160, Jan 2011.
- [25] L. Fu, M. Kilbinger, T. Erben, *et al.*, “CFHTLenS: cosmological constraints from a combination of cosmic shear two-point and three-point correlations,” *Monthly Notices of the Royal Astronomical Society*, vol. 441, pp. 2725–2743, Jul 2014.
- [26] J. Fluri, T. Kacprzak, A. Refregier, *et al.*, “Cosmological constraints from noisy convergence maps through deep learning,” *Phys. Rev. D*, vol. 98, p. 123518, Dec 2018.
- [27] D. Ribli, B. Armin Pataki, J. M. Zorrilla Matilla, *et al.*, “Weak lensing cosmology with convolutional neural networks on noisy data,” *arXiv e-prints*, p. arXiv:1902.03663, Feb 2019.
- [28] J. Fluri, A. Lucchi, T. Kacprzak, *et al.*, “Cosmological Parameter Estimation and Inference using Deep Summaries,” *arXiv e-prints*, p. arXiv:2107.09002, July 2021.
- [29] J. Fluri, T. Kacprzak, A. Lucchi, *et al.*, “Cosmological constraints with deep learning from kids-450 weak lensing maps,” *Phys. Rev. D*, vol. 100, p. 063514, Sep 2019.
- [30] T. L. Makinen, T. Charnock, J. Alsing, and B. D. Wandelt, “Lossless, Scalable Implicit Likelihood Inference for Cosmological Fields,” *arXiv e-prints*, p. arXiv:2107.07405, July 2021.
- [31] Kuijken, K., Heymans, C., Dvornik, A., *et al.*, “The fourth data release of the kilo-degree survey: ugri imaging and nine-band optical-ir photometry over 1000 square degrees,” *A&A*, vol. 625, p. A2, 2019.
- [32] R. J. Sgier, A. Réfrégier, A. Amara, and A. Nicola, “Fast generation of covariance matrices for weak lensing,” *Journal of Cosmology and Astroparticle Physics*, vol. 2019, p. 044, Jan. 2019.
- [33] R. Sgier, J. Fluri, J. Herbel, *et al.*, “Fast lightcones for combined cosmological probes,” *Journal of Cosmology and Astroparticle Physics*, vol. 2021, p. 047, Feb. 2021.
- [34] T. Kacprzak, J. Fluri, A. Schneider, *et al.*, “COSMOGRID: a fully numerical  $\Lambda$ CDM theory prediction for large scale structure cosmology,” *To be submitted to Journal of Cosmology and Astroparticle Physics*, 2022.
- [35] C. M. Hirata and U. c. v. Seljak, “Intrinsic alignment-lensing interference as a contaminant of cosmic shear,” *Phys. Rev. D*, vol. 70, p. 063526, Sep 2004.
- [36] S. Bridle and L. King, “Dark energy constraints from cosmic shear power spectra: impact of intrinsic alignments on photometric redshift requirements,” *New Journal of Physics*, vol. 9, pp. 444–444, dec 2007.
- [37] Joachimi, B., Mandelbaum, R., Abdalla, F. B., and Bridle, S. L., “Constraints on intrinsic alignment contamination of weak lensing surveys using the megaz-lrg sample,” *A&A*, vol. 527, p. A26, 2011.
- [38] A. Schneider and R. Teyssier, “A new method to quantify the effects of baryons on the matter power spectrum,” *Journal of Cosmology and Astroparticle Physics*, vol. 2015, p. 049, Dec. 2015.
- [39] A. Schneider, R. Teyssier, J. Stadel, *et al.*, “Quantifying baryon effects on the matter power spectrum and the weak lensing shear correlation,” *Journal of Cosmology and Astroparticle Physics*, vol. 2019, p. 020, Mar. 2019.
- [40] A. Schneider, S. K. Giri, S. Amodeo, and A. Refregier, “Constraining baryonic feedback and cosmology with weak-lensing, X-ray, and kinematic Sunyaev-Zeldovich observations,” *arXiv e-prints*, p. arXiv:2110.02228, Oct. 2021.
- [41] N. Perraudin, M. Defferrard, T. Kacprzak, and R. Sgier, “DeepSphere: Efficient spherical convolutional neural network with HEALPix sampling for cosmological applications,” *Astronomy and Computing*, vol. 27, p. 130, Apr. 2019.
- [42] T. Charnock, G. Lavaux, and B. D. Wandelt, “Automatic physical inference with information maximizing neural networks,” *Phys. Rev. D*, vol. 97, p. 083004, Apr 2018.
- [43] <http://kids.strw.leidenuniv.nl/>.
- [44] A. Edge, W. Sutherland, K. Kuijken, *et al.*, “The VISTA Kilo-degree Infrared Galaxy (VIKING) Survey: Bridging the Gap between Low and High Redshift,” *The Messenger*, vol. 154, pp. 32–34, Dec. 2013.
- [45] T. Erben, H. Hildebrandt, L. Miller, *et al.*, “CFHTLenS: the Canada-France-Hawaii Telescope Lensing Survey - imaging data and catalogue products,” *Monthly Notices of the Royal Astronomical Society*, vol. 433, pp. 2545–2563, Aug. 2013.
- [46] K. Begeman, A. N. Belikov, D. R. Boxhoorn, and E. A. Valentijn, “The Astro-WISE datacentric information system,” *Experimental Astronomy*, vol. 35, pp. 1–23, Jan. 2013.
- [47] L. Miller, C. Heymans, T. D. Kitching, *et al.*, “Bayesian galaxy shape measurement for weak lensing surveys - III. Application to the Canada-France-Hawaii Telescope Lensing Survey,” *Monthly Notices of the Royal Astronomical Society*, vol. 429, pp. 2858–2880, Mar. 2013.
- [48] I. Fenech Conti, R. Herbonnet, H. Hoekstra, *et al.*, “Calibration of weak-lensing shear in the Kilo-Degree Survey,” *Monthly Notices of the Royal Astronomical Society*, vol. 467, pp. 1627–1651, 01 2017.
- [49] N. Benítez, “Bayesian Photometric Redshift Estimation,” *The Astrophysical Journal*, vol. 536, pp. 571–583, June 2000.
- [50] Giblin, Benjamin, Heymans, Catherine, Asgari, Marika, *et al.*, “Kids-1000 catalogue: Weak gravitational lensing shear measurements,” *A&A*, vol. 645, p. A105, 2021.
- [51] K. M. Gorski, E. Hivon, A. J. Banday, *et al.*, “HEALPix: A framework for high-resolution discretization and fast analysis of data distributed on the sphere,” *The Astrophysical Journal*, vol. 622, pp. 759–771, apr 2005.
- [52] J. G. Stadel, *Cosmological N-body simulations and their analysis*. PhD thesis, UNIVERSITY OF WASHINGTON, 2001.
- [53] T. Tram, J. Brandbyge, J. Dakin, and S. Hannestad, “Fully relativistic treatment of light neutrinos in N-body simulations,” *Journal of Cosmology and Astroparticle Physics*, vol. 2019, p. 022, Mar. 2019.
- [54] J. Lesgourgues, “The Cosmic Linear Anisotropy Solving System (CLASS) I: Overview,” *arXiv e-prints*, p. arXiv:1104.2932, Apr. 2011.
- [55] J. Dakin, J. Brandbyge, S. Hannestad, *et al.*, “ $\nu$ CONCEPT: cosmological neutrino simulations from the non-linear Boltzmann hierarchy,” *Journal of Cosmology and Astroparticle Physics*, vol. 2019, p. 052, Feb. 2019.
- [56] D. Potter, J. Stadel, and R. Teyssier, “PKDGRAV3:



- beyond trillion particle cosmological simulations for the next era of galaxy surveys,” *Computational Astrophysics and Cosmology*, vol. 4, p. 2, May 2017.
- [57] A. Petri, Z. Haiman, and M. May, “Validity of the born approximation for beyond gaussian weak lensing observables,” *Phys. Rev. D*, vol. 95, p. 123503, Jun 2017.
- [58] H. Hildebrandt, J. L. van den Busch, A. H. Wright, *et al.*, “Kids-1000 catalogue: Redshift distributions and their calibration,” *Astronomy & Astrophysics*, vol. 647, p. A124, Mar 2021.
- [59] <https://github.com/LSSTDESC/CCL>.
- [60] C. G. R. Wallis, M. A. Price, J. D. McEwen, *et al.*, “Mapping dark matter on the celestial sphere with weak gravitational lensing,” *arXiv e-prints*, p. arXiv:1703.09233, Mar. 2017.
- [61] Wright, Angus H., Hildebrandt, Hendrik, van den Busch, Jan Luca, and Heymans, Catherine, “Photometric redshift calibration with self-organising maps,” *A&A*, vol. 637, p. A100, 2020.
- [62] A. H. Wright, H. Hildebrandt, J. L. van den Busch, *et al.*, “KiDS+VIKING-450: Improved cosmological parameter constraints from redshift calibration with self-organising maps,” *A&A*, vol. 640, p. L14, Aug. 2020.
- [63] M. P. van Daalen, J. Schaye, C. M. Booth, and C. D. Vecchia, “The effects of galaxy formation on the matter power spectrum: A challenge for precision cosmology,” *Mon. Not. Roy. Astron. Soc.*, vol. 415, pp. 3649–3665, 2011.
- [64] I. G. McCarthy, J. Schaye, S. Bird, and A. M. C. Le Brun, “The BAHAMAS project: Calibrated hydrodynamical simulations for large-scale structure cosmology,” *Mon. Not. Roy. Astron. Soc.*, vol. 465, no. 3, pp. 2936–2965, 2017.
- [65] N. E. Chisari *et al.*, “Modelling baryonic feedback for survey cosmology,” *Open J. Astrophys.*, 2019.
- [66] A. J. Mead, J. A. Peacock, C. Heymans, *et al.*, “An accurate halo model for fitting non-linear cosmological power spectra and baryonic feedback models,” *Monthly Notices of the Royal Astronomical Society*, vol. 454, pp. 1958–1975, Dec. 2015.
- [67] T. Tröster, C. Ferguson, J. Harnois-Déraps, and I. G. McCarthy, “Painting with baryons: augmenting N-body simulations with gas using deep generative models,” *Monthly Notices of the Royal Astronomical Society*, vol. 487, pp. L24–L29, July 2019.
- [68] G. Aricò, R. E. Angulo, C. Hernández-Monteagudo, *et al.*, “Modelling the large-scale mass density field of the universe as a function of cosmology and baryonic physics,” *Monthly Notices of the Royal Astronomical Society*, vol. 495, no. 4, pp. 4800–4819, 2020.
- [69] T. Lu and Z. Haiman, “The impact of baryons on cosmological inference from weak lensing statistics,” *Monthly Notices of the Royal Astronomical Society*, vol. 506, pp. 3406–3417, Sept. 2021.
- [70] T. Lu, Z. Haiman, and J. M. Zorrilla Matilla, “Simultaneously constraining cosmology and baryonic physics via deep learning from weak lensing,” *arXiv e-prints*, p. arXiv:2109.11060, Sept. 2021.
- [71] S. K. Giri and A. Schneider, “Emulation of baryonic effects on the matter power spectrum and constraints from galaxy cluster data,” *arXiv e-prints*, p. arXiv:2108.08863, Aug. 2021.
- [72] M. Sun, G. M. Voit, M. Donahue, *et al.*, “Chandra studies of the X-ray gas properties of galaxy groups,” *Astrophys. J.*, vol. 693, pp. 1142–1172, 2009.
- [73] A. Vikhlinin *et al.*, “Chandra Cluster Cosmology Project II: Samples and X-ray Data Reduction,” *Astrophys. J.*, vol. 692, pp. 1033–1059, 2009.
- [74] A. H. Gonzalez, S. Sivanandam, A. I. Zabludoff, and D. Zaritsky, “Galaxy Cluster Baryon Fractions Revisited,” *Astrophys. J.*, vol. 778, p. 14, 2013.
- [75] D. Eckert *et al.*, “The XXL Survey. XIII. Baryon content of the bright cluster sample,” *Astron. Astrophys.*, vol. 592, p. A12, 2016.
- [76] <https://github.com/deepsphere/deepsphere-cosmo-tf2>.
- [77] <https://www.cscs.ch/computers/piz-daint/>.
- [78] D. P. Kingma and J. Ba, “Adam: A Method for Stochastic Optimization,” *arXiv e-prints*, p. arXiv:1412.6980, Dec. 2014.
- [79] N. Srivastava, G. Hinton, A. Krizhevsky, *et al.*, “Dropout: A simple way to prevent neural networks from overfitting,” *Journal of Machine Learning Research*, vol. 15, no. 56, pp. 1929–1958, 2014.
- [80] D. Foreman-Mackey, D. W. Hogg, D. Lang, and J. Goodman, “emcee: The MCMC Hammer,” *PASP*, vol. 125, p. 306, Mar. 2013.
- [81] T. Tröster, M. Asgari, C. Blake, *et al.*, “KiDS-1000 Cosmology: Constraints beyond flat  $\Lambda$ CDM,” *A&A*, vol. 649, p. A88, May 2021.
- [82] A. F. Heavens, R. Jimenez, and O. Lahav, “Massive lossless data compression and multiple parameter estimation from galaxy spectra,” *Monthly Notices of the Royal Astronomical Society*, vol. 317, pp. 965–972, 10 2000.
- [83] Planck Collaboration, N. Aghanim, Y. Akrami, *et al.*, “Planck 2018 results. VI. Cosmological parameters,” *A&A*, vol. 641, p. A6, Sept. 2020.
- [84] S. P. D. Gill, A. Knebe, and B. K. Gibson, “The evolution of substructure - I. A new identification method,” *Monthly Notices of the Royal Astronomical Society*, vol. 351, pp. 399–409, June 2004.
- [85] S. R. Knollmann and A. Knebe, “AHF: Amiga’s Halo Finder,” *The Astrophysical Journal*, vol. 182, pp. 608–624, June 2009.

## Appendix A: Additional $\Omega_M - w_0$ Priors

The additional prior in the  $\Omega_M - w_0$  plane, mentioned in section IV A, is a consequence of the effective nature of the  $w$ CDM model along with the modeling of the relativistic fields according to [53]. The treatment of the relativistic fields requires a lookup table of transfer functions in the N-body gauge. The COSMOGRID generated the transfer functions with CLASS and then transformed them into the N-body gauge using CONCEPT. This gauge transformation requires the total velocity transfer function  $\vartheta_{\text{tot}}$ , which is defined as a weighted sum over the velocity transfer functions  $\vartheta_i$  from all relevant relativistic species  $i$ . The weight of each term is given by the sum of the density and pressure of the given species  $(\rho + p)_i$ . However, the normalization of the sum

$$(\rho + p)_{\text{tot}} = \sum_i (\rho + p)_i, \quad (\text{A1})$$

will perform a sign flip during the evolution if  $w_0 < -1$ . When this sign flip occurs, the total velocity transfer function diverges, similar to the phantom crossing for dark energy models, which results in impossibly large linear kicks inside the simulations. This divergence is inevitable for all models with  $w_0 < -1$ , however, it can occur in the future, i.e. at  $z < 0$ , for certain parameter choices, which makes it possible to run certain simulations with  $w_0 < -1$ . For  $w_a = 0$  and ignoring photons and neutrinos, the time of the divergence can be calculated via

$$a_{\text{divergence}} = \left( \frac{(\Omega_M - 1)(1 + w_0)}{\Omega_M} \right)^{\frac{1}{3w_0}}, \quad (\text{A2})$$

where  $\Omega_M = \Omega_{\text{cdm}} + \Omega_b$ . Using this formula we can select all parameters that are still possible to run with relativistic fields. We show the resulting additional prior in Figure 10.

## Appendix B: Accuracy of the Simulations

We compare the power spectra from all benchmark simulations to check the accuracy of the simulated convergence maps. Further, we also compare our fiducial configuration to spectra predicted with PYCCL using the whole range of the redshift distributions. The results of this comparison are shown in Figure 11. The power spectra of the benchmarks agree all well with each other and also with the PYCCL predictions. Meaning that the simulation settings have a negligible impact on the considered scales.

## Appendix C: Shell Baryonification

In this section we provide some details about our modified version of the baryon correction model from [39]

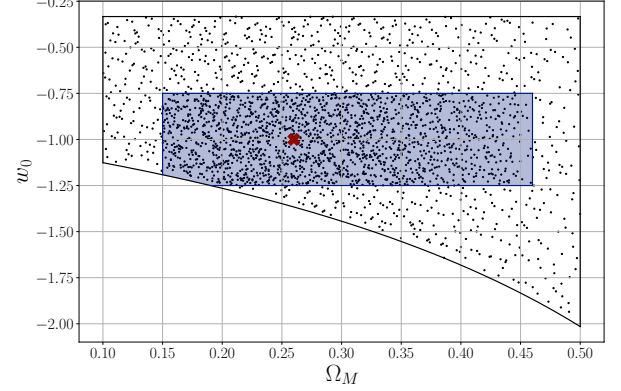


FIG. 10. The 2'500 grid points projected onto the  $\Omega_M - w_0$  plane. The lower border indicates the additional prior from equation A2 and the shaded region corresponds to the tight prior mentioned in section IV A. The red cross in the middle indicates the fiducial cosmology.

which we dub *shell baryonification*. The original correction model starts with the assumption that the dark-matter-only halos are well described by combining the truncated Navarro-Frenk-White (NFW) profile with a 2-halo density component

$$\rho_{\text{dmo}}(r) = \rho_{\text{nfw}}(r) + \rho_{2\text{h}}(r). \quad (\text{C1})$$

This profile only depends on the cosmological parameters of the simulations, the viral mass of the halo  $M \equiv M_{200}$  and the concentration  $c \equiv c_{200}$ . However, a more realistic description of the profile would also include gas, the central galaxy and a collisionless matter component

$$\rho_{\text{dmb}}(r) = \rho_{\text{gas}} + \rho_{\text{cga}}(r) + \rho_{\text{clm}}(r) + \rho_{2\text{h}}(r). \quad (\text{C2})$$

The goal of the correction model is now to transform the dark matter only profile  $\rho_{\text{dmo}}$  from the simulations into a profile that includes this baryonic feedback  $\rho_{\text{dmb}}$ . This is done by matching the halo masses

$$M_\chi(r) = 4\pi \int_0^r s^2 \rho_\chi(s) ds. \quad (\text{C3})$$

The halo mass functions  $M_{\text{dmo}}(r)$  and  $M_{\text{dmb}}(r)$  are bijective function, making it possible to invert them. The difference between the inverted function gives rise to the displacement function

$$d(r_{\text{dmo}}|M, c) = r_{\text{dmb}}(M) - r_{\text{dmo}}(M), \quad (\text{C4})$$

for each halo with mass  $M$  and concentration  $c$ . Each particle inside the simulation that is close enough to a halo, is then displaced using this function, transforming the dark matter only profiles  $\rho_{\text{dmo}}$  into  $\rho_{\text{dmb}}$ . The model requires that the simulation is run in snapshot mode, such that the position of each particle is known. However, the simulations of the COSMOGRID were run in lightcone

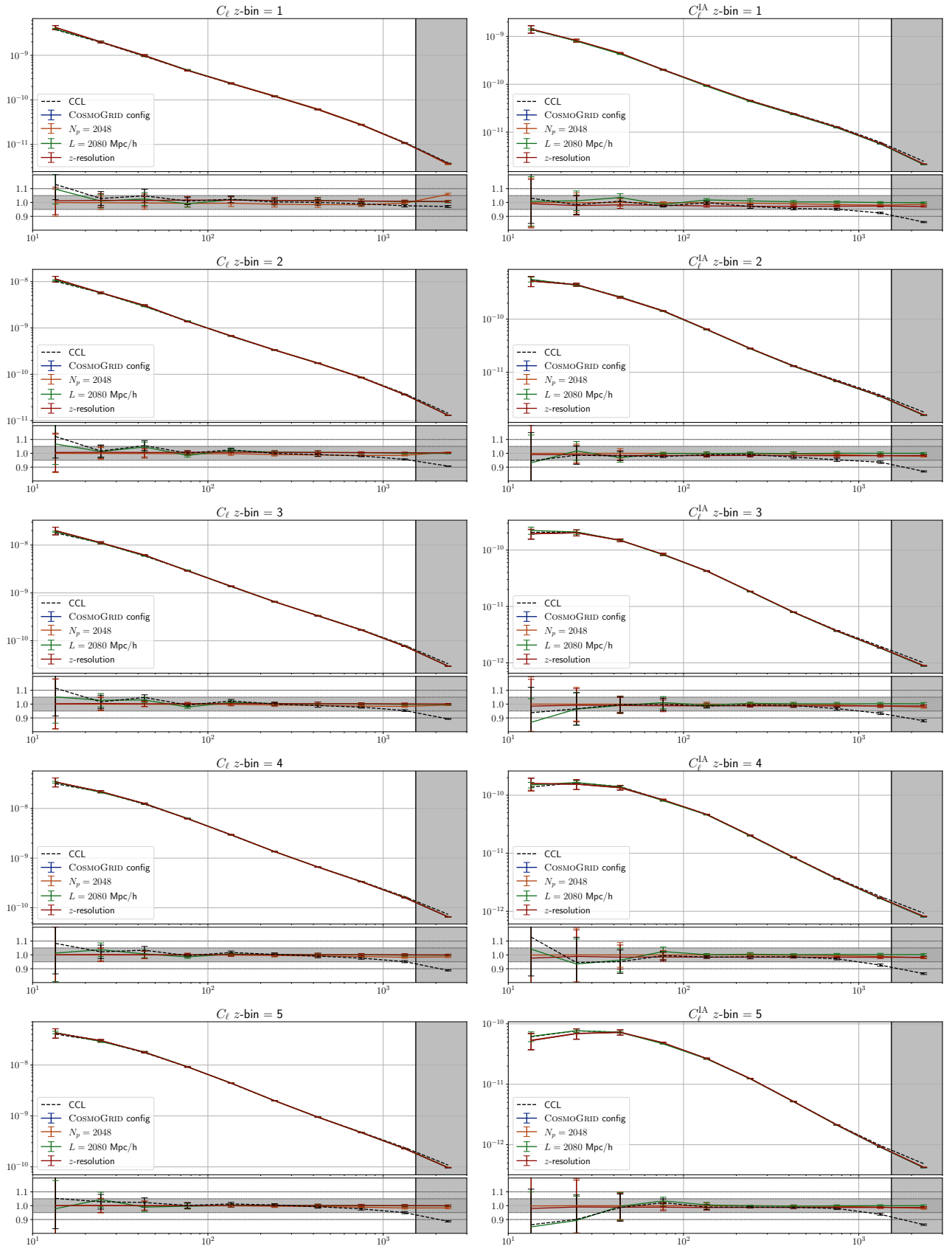


FIG. 11. Power spectra comparison of PyCCL and the benchmark simulations. The spectra are all calculated using maps with an  $n_{\text{side}}$  of 2048 to avoid resolution effects. The left column shows the spectra of the cosmological signal for each redshift bin. The right column shows the same comparison for the intrinsic alignment (II) spectra. The shaded regions on the right side of each plot indicate the scales that can't be resolved with our fiducial resolution of  $n_{\text{side}} = 512$ . The lower panels of each plot show the ratio of the COSMOGRID settings with respect to the other settings.

mode and only particle shells are available along with the halo catalogues of each time step, making it impossible to directly apply this correction model.

The halo catalogues of the COSMOGRID were generated using a FoF halo finder with a linkage length of 20% of the mean particle separation and were generated for each time step. For our correction model we used all FoF halos that contain at least 100 particles within the virial radius  $r \equiv r_{200}$ . We fit a standard NFW profile to each halo using the logarithmically binned mass shells contained in the COSMOGRID halo catalogues to obtain the concentration  $c$  and mass  $M$  of each halo. Afterwards, we organized the halos into shells using the same shell boundaries and replication schemes as in the original lightcone mode. Halos that were closer than 20 Mpc to a shell boundary are assigned to both shells of the boundary, making it possible for them to affect the particles in both shells. Following the UFALCON convention, we assume that all halos and particles inside a shell lie at the shells mean redshift  $z_m$ . Next we define the projected halo mass function

$$M_\chi^p(r) = 2\pi \int_0^r s \int_0^{z_{\max}} \rho_\chi(s, z) dz ds, \quad (\text{C5})$$

which corresponds to the mass function of a halo that was projected onto a plane. We chose  $z_{\max} = 50r$  as the limit of the integration. Note that the projected mass is actually diverging as  $z_{\max}$  increases, because of the 2-halo component. However, the projected displacement function

$$d^p(r_{\text{dmo}}|M, c) = r_{\text{dmb}}(M^p) - r_{\text{dmo}}(M^p), \quad (\text{C6})$$

is always finite, because the divergent terms cancel out. The shell baryonification is then performed by displacing the pixels of the high resolution shells ( $n_{\text{side}} = 2048$ ) of the COSMOGRID simulations. For each halo we assume a locally flat sky and displace the pixels closer than  $50r$  using the projected displacement function. Afterwards, we assign new values to the HEALPix pixel positions using a linear interpolation to the displaced pixels. In a last step, we decrease the resolution of the shells to our final resolution of  $n_{\text{side}} = 512$  which acts as a smoothing kernel.

We compare the power spectra of maps generated with the original baryon correction model and our shell baryonification in Figure 12. The shell baryonification was performed as explained above using a random fiducial simulation and our fiducial baryonic correction parameters (see section IV E 4 and table I). The original baryonification model was performed in the same way as in F19, which is the normal procedure as described in [39]. We reran the simulation with the identical initial condition in snapshot mode. Afterwards, we used the AMIGA halo finder [84, 85] to identify all relevant halos and performed the normal baryon corrections inside the generated snapshots. Finally, we generate the shells of the past lightcone using the replication scheme of the original simulations and project them with UFALCON and the fiducial redshift

distributions. The power spectra of the resulting maps is shown in Figure 12. Both approaches agree very well over all considered scales. Additionally to the two baryonic feedback models, we also plot the power spectrum of the maps without any corrections. One can clearly see that there is a significant drop of the power on small scales (high  $\ell$ -modes) for the baryon-corrected maps.

## Appendix D: Additional Network Benchmarks

In this appendix we provide more details about the benchmark networks. These networks are used to test the robustness of the pipeline with respect to certain hyperparameters of the used networks.

### 1. Architectures & Training

Besides the fiducial architecture presented in section IV F, we train three different networks. The first network has the identical architecture as the fiducial networks, however, it was trained on 16 GPUs instead of eight, leading to a total batch size that is twice as big as the fiducial one. For the second benchmark model we doubled the number of residual layers. And for the last benchmark model we replaced the graph convolutional layers (GCL) inside the residual layers with standard 1D convolutional layers. The GCL of DEEPSHARE have the major advantage that they are approximately rotational equivariant. However, a potential disadvantage is that they only connect pixels in a certain neighborhood. This means that the disconnected patches of the KiDS-1000 data might not be correlated if one applies only GCL layers. This does not happen in our networks since we also apply normalization layers that affect all pixels, however, it might still decrease the performance. Standard 1D convolution are not rotational equivariant, however, they automatically connect the disconnected patches of the KiDS-1000 data. We apply 1D convolutions on the HEALPix pixel arrays with a filter size of 16. Besides the mentioned changes, all other parameters, e.g. initial layers or optimizer settings remained unchanged. In the next section we will show the impact of these choices on the constraints of the degeneracy parameter.

### 2. Constraints

We present the constraints on the degeneracy parameter for various settings in Figure 13. All constraints are generated as described in sections IV H and V, using a kernel scale of  $h = 0.4$  and we used the fiducial benchmark simulations as mock observations. It can be seen that the constraints of all settings are very consistent. The fiducial constraints from section V are the tightest because they represent the combination of six networks. Besides that, all other settings have a very similar performance,



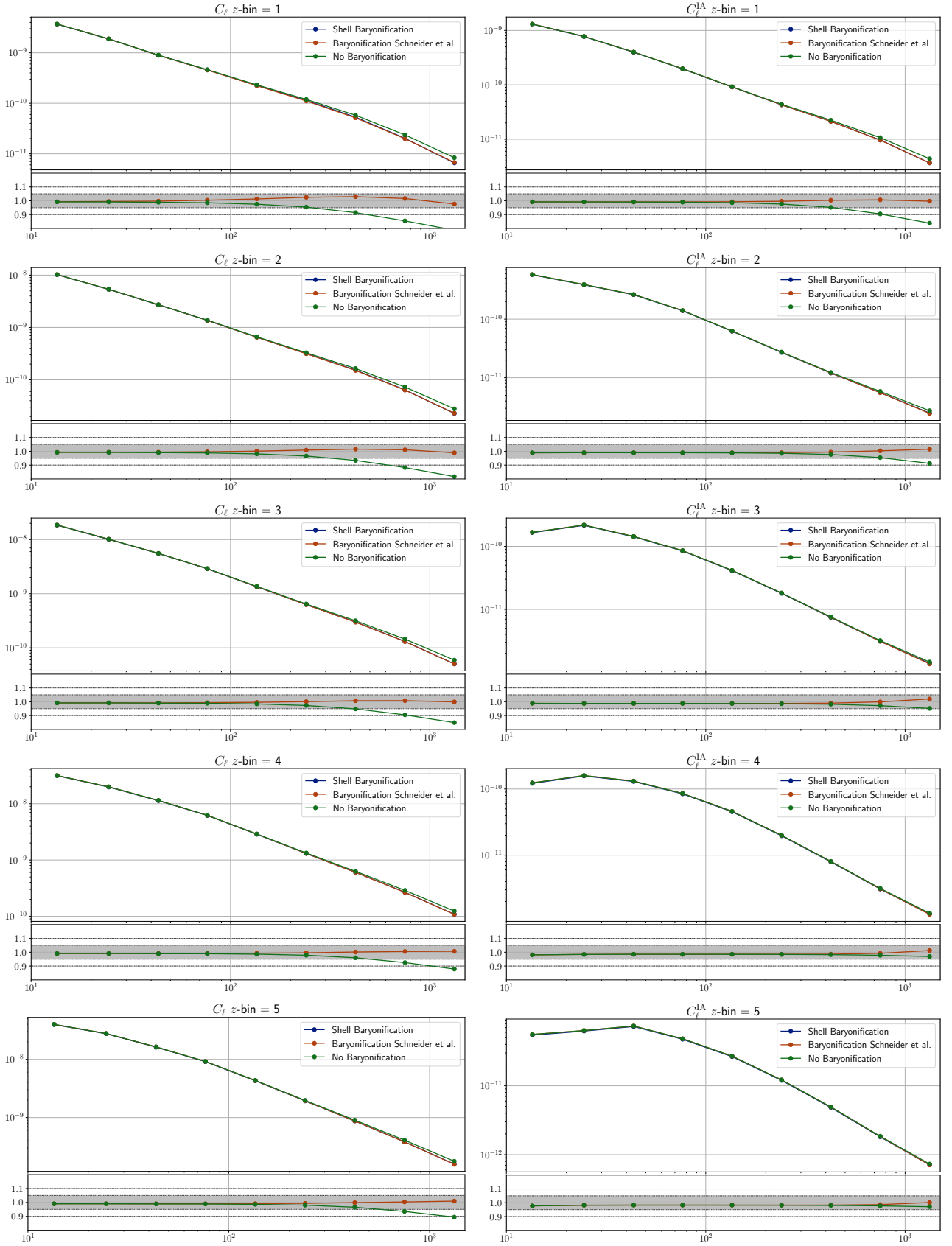


FIG. 12. Power spectra of the shell baryonification, the original baryonification from [39], and the dark-matter-only-case using a fiducial simulation. The left-hand column shows the power spectra of the signal for each redshift bin and the right-hand column for the intrinsic alignment maps (II).

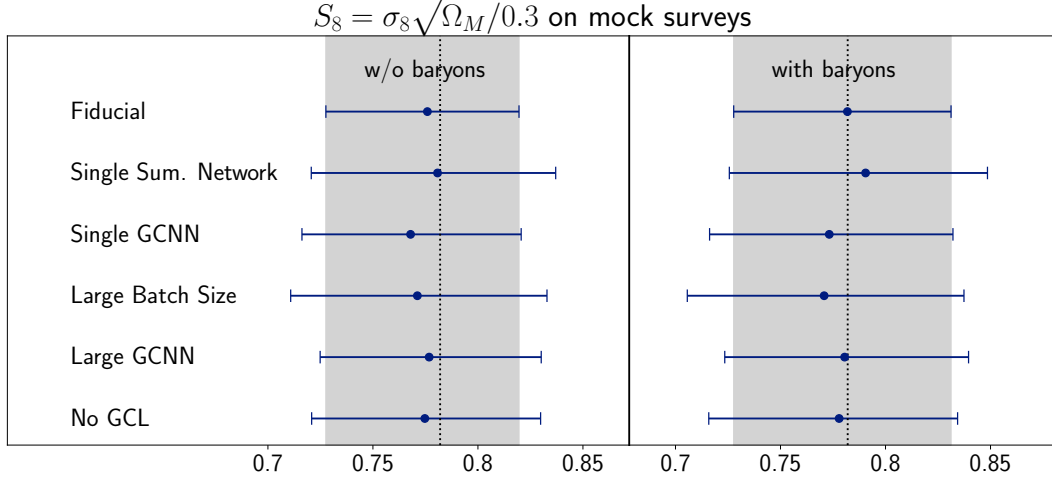


FIG. 13. Constraints of various different settings using the fiducial benchmark simulations as mock observation. The first constraint “Fiducial” is equivalent to the fiducial network constraints of Figure 5 and serves as reference point. The left side of the plot shows the constraints without baryonic correction, while the right side includes these corrections.

Type	Baryons	$\Omega_M$	$\sigma_8$	$h_0$	$\Omega_b$	$n_s$	$w_0$	$A_{IA}$	$S_8$
GCNN	no	$0.262^{+0.048}_{-0.162}$	$0.884^{+0.136}_{-0.277}$	$0.725^{+0.095}_{-0.085}$	$0.045^{+0.015}_{-0.015}$	$0.962^{+0.031}_{-0.092}$	$-0.930^{+0.316}_{-0.285}$	$0.514^{+0.670}_{-0.663}$	$0.774^{+0.043}_{-0.048}$
GCNN	yes	$0.259^{+0.046}_{-0.159}$	$0.903^{+0.149}_{-0.286}$	$0.726^{+0.094}_{-0.086}$	$0.045^{+0.015}_{-0.015}$	$0.966^{+0.104}_{-0.096}$	$-0.891^{+0.335}_{-0.297}$	$0.457^{+0.673}_{-0.665}$	$0.786^{+0.046}_{-0.055}$
GCNN Optimized	no	$0.251^{+0.041}_{-0.151}$	$0.903^{+0.144}_{-0.268}$	$0.721^{+0.028}_{-0.081}$	$0.046^{+0.014}_{-0.016}$	$0.958^{+0.028}_{-0.088}$	$-0.923^{+0.289}_{-0.268}$	$0.479^{+0.542}_{-0.542}$	$0.776^{+0.037}_{-0.044}$
GCNN Optimized	yes	$0.239^{+0.037}_{-0.130}$	$0.940^{+0.188}_{-0.228}$	$0.722^{+0.028}_{-0.082}$	$0.045^{+0.015}_{-0.015}$	$0.966^{+0.054}_{-0.068}$	$-0.854^{+0.304}_{-0.279}$	$0.423^{+0.492}_{-0.488}$	$0.793^{+0.039}_{-0.051}$
Power Spectrum	no	$0.259^{+0.047}_{-0.154}$	$0.874^{+0.150}_{-0.253}$	$0.726^{+0.094}_{-0.086}$	$0.045^{+0.015}_{-0.015}$	$0.967^{+0.103}_{-0.097}$	$-0.884^{+0.329}_{-0.298}$	$0.774^{+0.856}_{-0.705}$	$0.765^{+0.053}_{-0.052}$
Power Spectrum	yes	$0.261^{+0.055}_{-0.145}$	$0.886^{+0.156}_{-0.265}$	$0.728^{+0.092}_{-0.088}$	$0.045^{+0.015}_{-0.015}$	$0.969^{+0.101}_{-0.099}$	$-0.843^{+0.410}_{-0.243}$	$0.734^{+0.883}_{-0.700}$	$0.779^{+0.061}_{-0.059}$

TABLE IV. Full parameter constraints of our analysis. We present the constraints of all setting presented in section VI with and without the treatment of baryon corrections.

indicating that our results are fairly robust with respect to the hyperparameter choices.

### Appendix E: Full Parameter Constraints

We present the constraints on all cosmological parameters in table IV. It is important to note that most of

the constraints are dominated by their prior distribution (see table I), which is why we did not include them in the main paper. The only parameters with meaningful constraints are the degeneracy parameter  $S_8$  and the intrinsic alignment amplitude  $A_{IA}$ . Nevertheless, all results are consistent with each other.